Structure of the human lipid exporter ABCB4 in a lipid environment

Olsen, Jeppe A ; Alam, Amer ; Kowal, Julia ; Stieger, Bruno ; Locher, Kaspar P

Abstract: ABCB4 is an ATP-binding cassette transporter that extrudes phosphatidylcholine into the bile canaliculi of the liver. Its dysfunction or inhibition by drugs can cause severe, chronic liver disease or drug-induced liver injury. We determined the cryo-EM structure of nanodisc-reconstituted human ABCB4 trapped in an ATP-bound state at a resolution of 3.2 Å. The nucleotide binding domains form a closed conformation containing two bound ATP molecules, but only one of the ATPase sites contains bound Mg2+. The transmembrane domains adopt a collapsed conformation at the level of the lipid bilayer, but we observed a large, hydrophilic and fully occluded cavity at the level of the cytoplasmic membrane boundary, with no ligand bound. This indicates a state following substrate release but prior to ATP hydrolysis. Our results rationalize disease-causing mutations in human ABCB4 and suggest an 'alternating access' mechanism of lipid extrusion, distinct from the 'credit card swipe' model of other lipid transporters.

DOI: https://doi.org/10.1038/s41594-019-0354-3

Originally published at:
Olsen, Jeppe A; Alam, Amer; Kowal, Julia; Stieger, Bruno; Locher, Kaspar P (2020). Structure of the human lipid exporter ABCB4 in a lipid environment. Nature Structural Molecular Biology, 27(1):62-70.
DOI: https://doi.org/10.1038/s41594-019-0354-3

Structure of the human lipid exporter ABCB4 in a lipid environment

Jeppe A. Olsen[1], Amer Alam[1,2], Julia Kowal[1], Bruno Stieger[3] and Kaspar P. Locher[1,*]

*Author Affiliations: 1: ETH Zürich, Department of Biology, Institute of Molecular Biology and Biophysics, Otto-Stern-Weg 5, 8093 Zürich, Switzerland. 2: Present address: The Hormel Institute, University of Minnesota, 801 16th Ave NE, Austin, MN 55912-3679, USA. 3: University Hospital Zürich, Department of Clinical Pharmacology and Toxicology, Rämistrasse 100, 8091 Zürich. *Corresponding author, e-mail address: locher@mol.biol.ethz.ch*

ABCB4 is an ATP-binding cassette transporter that extrudes phosphatidylcholine into the bile canaliculi of the liver. Its dysfunction or inhibition by drugs can cause severe, chronic liver disease or drug-induced liver injury. The molecular mechanisms underpinning the physiological function of ABCB4 and its inhibition by small-molecule compounds are unknown. We determined the cryo-EM structure of nanodisc-reconstituted human ABCB4 trapped in an ATP-bound state at a resolution of 3.2 Å. The nucleotide-binding domains form a closed conformation containing two bound ATP molecules, but only one of the ATPase sites contained bound Mg^{2+}. The transmembrane domains adopt a collapsed conformation at the level of the lipid bilayer, but we observed a large, hydrophilic, and fully occluded cavity at the level of the cytoplasmic membrane boundary, with no ligand bound. This indicates a state following substrate release but prior to ATP-hydrolysis. Mutational analysis suggested a surprising, essential role of the extracellular loops in phosphatidylcholine transport. We further identified three residues on transmembrane helix 12 that are critical for function and may be involved in substrate recognition. Our results rationalize disease-causing mutations in human ABCB4 and provide evidence for an 'alternating access' mechanism of lipid extrusion, distinct from the 'credit card swipe' model of other lipid flippases and scramblases.

The ATP-binding cassette (ABC) transporter ABCB4 is a phospholipid translocator critical for bile generation[1-3]. It is expressed mainly in hepatocytes[4,5] and trafficked to the apical membranes forming the boundary to bile canaliculi. ABCB4 actively exports phosphatidylcholine (PC) into the bile and its functional role is closely connected with the functions of two other ABC transporters, the bile salt export pump BSEP (ABCB11) and the cholesterol transporter ABCG5/G8[2,3]. The PC extrusion of ABCB4 is stimulated by canalicular bile salts (exported by ABCB11) and in turn stimulates the cholesterol export mediated by ABCG5/G8. Balancing these three transport processes is essential to guarantee the correct ratio of bile constituents forming mixed micelles, which in turn is important to protect the liver and bile ducts from the detergent-like activity of bile salts[1-3] (Fig. 1a).

Several mutations in the *ABCB4* gene are known to cause progressive familial intrahepatic cholestasis (PFIC) type 3, a severe liver disease[6]. Less severe, or shorter term, functional impairments of ABCB4 are associated with higher risk of gall stones, intrahepatic cholestasis of pregnancy and are a risk factor for developing cholangitis[6-8]. Several ABCB4 mutations have been studied in cellular assays and in sufficient detail to distinguish whether they affect the function of the transporter or either protein expression or trafficking([9-15]). In addition to genetic mutation, ABCB4 can be inhibited by pharmaceutical compounds, which can cause drug-induced liver injury (DILI)[16,17]. Several marketed drugs with DILI risk profiles inhibit ABCB4 in cellular assays[18-20], and ABCB4 inhibition by Itraconazole has been shown to cause cholestasis in

rats[21]. Further, genomic studies suggest a link between ABCB4 dysfunction and hepatobiliary malignancies[22-25], and it has been reported that *ABCB4* is frequently epigenetically silenced in cancer[26].

Despite its importance in health and disease, no high-resolution structure of ABCB4 is currently available. Furthermore, the significant mechanistic diversity within the ABC transporter family make mechanistic inferences based on other ABC transporters problematic in the absence of direct structural data[27]. ABCB4 has been proposed to work by 'flopping' PC molecules from the inner to the outer membrane leaflet[28,29], where the resulting excess of outer leaflet PC is released into canalicular bile in a process facilitated by canalicular bile salts[30]. However, it is not known how ABCB4 achieves the translocation and reorientation of PC or whether the release of PC is into the outer membrane leaflet or directly into bile. Furthermore, other ABC transporters of lipidic substrates traffic these in a variety of ways, with distinct mechanisms proposed for MsbA[31], PglK[32], and ABCA1[33].

When first discovered, ABCB4 was assumed to be a multi-drug exporter due to its high sequence conservation (76% identity, 86% similarity) to ABCB1[34] (P-glycoprotein), and ABCB4 is still often referred to as multidrug-resistance-protein 3 (MDR3). However, while various studies have shown ABCB4 to be capable of recognizing and transporting some ABCB1 substrates (albeit with low capacity)[35,36], the data regarding its role in conferring drug resistance is inconclusive[37-40]. Similarly, ABCB1 has only been shown to flip short-chain, fluorescently labelled lipid analogues in cellular assays[41], and despite its canalicular expression[3], ABCB1 is unable to compensate for loss of ABCB4 function[1]. Consequently, it is now accepted that despite their high sequence identity, ABCB4 and ABCB1 are functionally distinct proteins[2,42]. However, while multiple structures of ABCB1 have been reported and have increased our mechanistic understanding of multi-drug export[43-46], they are insufficient to decipher the molecular details of ABCB4-catalyzed phosphatidylcholine transport. Direct visualization of ABCB4 has been challenging, partly due to difficulties in obtaining suitable amounts of functional and pure ABCB4[47], possibly stemming from toxicity induced by its overexpression in mammalian cells[48]. This has also hampered efforts at purifying the protein, likely explaining the limited number of *in vitro* studies on purified ABCB4[42,49,50].

In order to address the lack of mechanistic insight into ABCB4 function, rationalize disease-causing mutations, and lay the groundwork for structure-guided therapeutic strategies, we purified ABCB4 from human cells and determined its structure at a resolution of 3.2Å. This allowed us to generate structure-guided chimeras between ABCB4 and ABCB1, which in turn allowed us to identify key differences responsible for the functional distinction between the two transporters. Based on these results we propose that ABCB4 employs an 'alternating access' mechanism for PC translocation, with an important component being that PC export critically depends on the extracellular loops.

Results

Functional characterization of ABCB4

For ABCB4 expression, we generated a tetracycline-inducible, stable HEK293 cell line, where the function of expressed hABCB4 could be tested in a cellular PC extrusion assay. To mimic the physiological conditions of endogenous ABCB4, taurocholate was added to stimulate PC transport, and BSA was added as an acceptor of extruded lipids. (Fig. 1a-b). While this assay does not replicate the polarity of hepatocytes or the complexity of bile that contains mixed micelles consisting of an array of bile salts and PC, we were able to demonstrate that PC extrusion in our ABCB4-generating cell line was dependent on induction of ABCB4 expression, and that PC extrusion was stimulated more than two-fold by the presence of taurocholate (Fig. 1b). The extrusion activity was completely absent in a similar cell line expressing ABCB4 with glutamate to glutamine (EQ) mutations in both Walker-B motifs[51]. These EQ mutations strongly reduce the ATPase activity of ABC transporters and allow trapping them in a pre-hydrolytic state[52]. The absence of PC extrusion by ABCB4[EQ] despite higher protein yields over wildtype ABCB4 (Supp. Fig. 1), demonstrated that the ABCB4-mediated PC extrusion we observed was dependent on sustained ATP hydrolysis.

ABCB4 extracted from the membrane and purified in detergent micelles displayed very low ATPase activity (Fig. 1d, red line). Earlier studies arriving at similar results led to the proposal that low-efficiency, low-affinity transport may be an adaptation to the special circumstances of ABCB4 in the canaliculi[35,47], where the protein is essentially suspended in its own substrate. However, other studies have found ample ATPase activity of ABCB4[15,50]. We reconstituted detergent-purified ABCB4 into nanodiscs containing a mixture of liver polar lipids and cholesteryl hemisuccinate (Fig. 1c, Supp. Fig. 1c-f) and recovered robust ATP hydrolysis activity, with V_{max} in the range of 80-130 nmol ATP min^{-1} mg^{-1} and K_m for ATP in the range of 0.6-1.2mM (Fig. 1d blue curve), lower than the 200-400 nmol ATP min^{-1} mg^{-1} found for nanodisc-reconstituted ABCB1[45]. Similar to ABCB1[53], the ATPase activity of ABCB4 was all but abolished by addition of ortho-vanadate (Supp. Fig. 2a), and we found little to no activity for ABCB4[EQ] in detergent or in nanodiscs (Fig. 1e). Our results demonstrate that the environment of human ABCB4 is critical for its activity, perhaps due to the presence of PC in the nanodiscs, which suggests that nanodisc-reconstituted ABCB4 is in a physiologically relevant state for structural studies.

Cryo-EM structure determination of ATP-bound ABCB4[EQ]

Our first attempts at determining the structure of ABCB4 were performed using nanodisc reconstituted wild-type protein stabilized by vanadate-trapping. However, the resulting reconstructions displayed low resolution that did not allow transmembrane helices to be unambiguously resolved, while multiple NBD conformations with varying degrees of NBD closure were observed (Supp. Fig. 2b-d). We concluded that there was high conformational flexibility and residual movement in the protein despite the vanadate

trapping, and that another approach for conformational stabilization was necessary. We next studied nanodisc-reconstituted ABCB4[EQ] in the presence of 5mM ATP-Mg^{2+} (Supp. Fig. 3a). The resulting 2D and 3D class averages showed that a majority of particles adopted a closed NBD conformation (Supp. Fig. 3b). However, a significant minority adopted a state resembling the 'inward open' conformation, the density of which was visibly worse than that of the closed conformation (Supp. Fig. 3b). The fraction of particles in the open conformation (29%) is reasonably close to the value of ~10-20% unoccupied particles expected for a protein with a K_m of 0.6-1.2 mM in the presence of 5mM ATP-Mg^{2+}, assuming a Hill slope of one in the Hill-Langmuir equation. The discrepancy could suggest that the true Hill-slope has a slightly different value due to the presence of two ATP binding sites in the transporter. Particles showing closed NBDs were used to obtain a 3D reconstruction at a resolution of 3.2Å as judged by the FSC curve using the 0.143 cutoff[54] (Supp. Fig. 3c), allowing for unambiguous side chain placement for most of the protein (Supp. Fig. 4).

The 'closed conformation' of ABCB4[EQ] is incompatible with substrate binding

The structure of ABCB4[EQ] in a nucleotide-bound state (Fig.2 a-b) is characterized by extensive contacts between the two halves of the transporter along the entire vertical axis (perpendicular to the membrane) (Fig. 2b-c). The transmembrane domains (TMDs) are surrounded by two rings of ordered cholesterol molecules bound to lipid-exposed surface grooves, forming both hydrogen bonds and aromatic stacking (Fig. 2b), reminiscent of interaction patterns observed for nanodisc-reconstituted ABCB1[45]. At the level of the lipid bilayer, the TMDs adopted a collapsed conformation, with no cavity visible. In contrast, a large hydrophilic cavity was observed at the boundary of the inner leaflet, extending into the cytoplasmic regions of the TMDs. This cavity is completely closed off from the intracellular matrix and from the extracellular domain of ABCB4 (Fig. 2c). Despite the size of this cavity (3756 $Å^3$ estimated in Caver[55] with a probe size of 1.4Å) no extraneous density was found inside (size of a PC molecule, PC7 from PDBeChem[56], estimated at 782 $Å^3$ in UCSF Chimera[57]). The hydrophilic nature and the location mainly below the membrane level make this pocket an unlikely site for lipidic substrate binding. However, it may provide a site for binding inhibitors or modulators of ABCB4.

The absence of any opening of the hydrophobic interior to either side of the membrane differentiates our structure from both the 'inward-open' conformation observed for several ABC transporters, including ABCB1[43], the 'outward open' conformation observed for Sav1866[58], and the occluded conformation observed for McjD[59]. The finding that ABCB4 is substrate-free despite the high concentration of substrate in the lipidic nanodisc suggests that the observed state is incompatible with substrate binding and that the ATP-triggered transition into this state is likely responsible for causing the extrusion of previously associated PC molecules. Our structure therefore indicates that transport of PC by ABCB4 precedes

hydrolysis and that the energy supplied by conversion of ATP to ADP is required to 'reset' the protein for the next transport cycle, suggesting an 'ATP switch' model[51] for ABCB4 function, similar to what has been proposed for ABCB1[46]

Subtle asymmetry in interactions of NBDs with ATP-Mg^{2+}

We observed strong and well-defined EM density for two bound ATP molecules sandwiched between the Walker-A motifs and the Signature motifs of opposing NBDs (Fig. 3a). At ATPase site 1 (defined as the site containing the Walker-A and Walker-B motifs of NBD2 and the Signature Motif of NDB1), clear density is observed for bound ATP-Mg^{2+}, with the magnesium ion mediating strong contacts between the beta and gamma phosphates of ATP and residues S1076 (in the Walker A motif) and the Q-loop glutamine, Q1117, near the Signature motif of NBD1 (Fig. 3a, right insert). In contrast, the other ATPase site (site 2, Fig. 3a, left insert) shows no density for a bound magnesium ion, and the gamma phosphate moiety of bound ATP is shifted towards Q477 and S436 (Fig. 3b). The density for these residues and for the gamma phosphate group of ATP are slightly weaker than the equivalent densities in ATPase site 1, suggesting that bound Mg^{2+} helps orient and immobilize the phosphate groups. Another possible interpretation of the observed asymmetry would be that instead of ATP, ADP-Mg^{2+} could be bound at the ATPase site 2. However, this would imply that during sample preparation, all ATP at site 2 had been hydrolysed. However, given the near absence of hydrolysis of the ABCB4[EQ] sample, it is much more likely that ATP is bound at site 2. We also observe asymmetry in the so-called H-loops containing the conserved H589 (near site 1) and H1231 (near site 2). Equivalent histidines have been shown to be essential for ATP hydrolysis in the ABC transporter HlyB[60]. While the different conformations of H589 and H1231 of ABCB4 do not appear to affect the overall structure of the NBDs, they might influence hydrolysis and be in part responsible for the significantly lower ATPase rates of ABCB4 compared with ABCB1.

While asymmetry is an intrinsic feature in heterodimeric ABC transporters that contain one consensus and one degenerate ATPase site[27], it has also been proposed to be relevant for transporters containing two functional ATPase sites including ABCB1[61], where nucleotide trapping experiments suggest that hydrolysis occurs at both sites but does not occur simultaneously[52,62]. Remarkably, no asymmetry was observed in the nucleotide-bound structure of ABCB1[EQ] or in other full-length ABC transporter structures featuring EQ mutations[63-65]. For ABCB1, this was ascribed to the use of an EQ-mutation and of saturating concentration of ATP-Mg^{2+} (10mM against a K_m of 0.18mM)[46]. Thus, our ABCB4 structure is the first report of an ABC transporter containing two consensus ATPase sites but structural asymmetry at the ATPase sites of a double EQ variant. Our results may support the idea that even for ABC transporters with very similar NBDs such as ABCB1 and ABCB4, subtle but significant differences in how the NBDs interact with nucleotides may occur at lower saturation (5mM against a K_m of 0.6-1.2mM). Since the average

intracellular concentration of ATP in rat liver has been estimated to be ~3.5mM[66], the concentration used here may be close to the physiological working conditions of ABCB4. However, we cannot rule out that the asymmetry we observe is influenced by, or even caused by, the EQ mutations. The function of ABCB4 containing a single EQ mutation (E558Q) has been investigated previously. The introduced mutation affected ATPase site 2, leaving site 1, where we observe bound Mg^{2+}, unaltered. It was found that the single EQ mutation of ABCB4[E558Q] abolished the transport of PC[10], demonstrating that the ATPase site where we find bound Mg^{2+} cannot drive transport alone. Unravelling the precise effects of this structural asymmetry, for example alternating hydrolysis, will likely require alternate conformations to be investigated at high resolution.

Disease-causing mutations suggest mechanistic conservation between ABCB4 and ABCB1

We used our structure to rationalize the array of known disease-causing ABCB4 mutations and as a starting point for functional studies of the molecular determinants of PC transport. The available literature[9-15] reported 15 unique positions where ABCB4 mutation did not significantly impair protein expression or maturation but did impair its function (Fig. 4a, Supp. Table 2), ranging in severity from moderate to complete impairment. Though the number of mutations under consideration is thus limited and mutations from patients suffering from PFIC appear predominant, some intriguing patterns emerged. A cluster of positions associated with functionally impairing, disease-causing mutations is seen in the NBDs (Fig. 4a, Supp. Fig. 6 for stereo view), with all these positions except A1186T less than 5Å from a bound nucleotide, suggesting that they interfere with ATP binding. In addition, 11 mutations were reported to impair expression, trafficking or maturation of ABCB4 (Fig. 4b, Supp. Fig. 6 for stereo view). They also display clustering in the NBDs but based on their location only G536R would be expected to disrupt ATP binding directly. This is particularly interesting because the PC secretion activity of the G536R mutation was partially rescued by the CFTR potentiator Ivacaftor, as was the functional impairment of the mutations G535D, S1076C, S1176L and S1178S. Our structure provides direct evidence of a previous proposal based on homology modelling that these mutations would all affect the nucleotide binding sites[13], suggesting that the potential success of treatment of ABCB4 deficiency by Ivacaftor might be predicted based on knowledge of a patient's genotype.

For disease-causing mutations in the TMDs, three mutations (P726L, S346I and A286V) were reported to lead to more than 90% functional impairment, without affecting trafficking. They interact with residues in the core of ABCB4, which can explain why their disruption is particularly damaging. The remaining positions have side chains oriented towards the membrane or solvent-exposed areas and have less drastic effects on function when mutated. Interestingly, even P726, S346 and A286 are conserved in ABCB1, as are nearly all the positions where functionally impairing mutations are found, the exceptions being T34

and A737 (Supp. Fig. 5). This is surprising because it is precisely in their function that these two ABC transporters differ, but suggests that ABCB4 and ABCB1 achieve their distinct functions through a similar transport mechanism.

ABCB4-ABCB1 chimeras reveal function-encoding regions of ABCB4

In order to identify which protein regions are responsible for the distinct functions of ABCB4 and ABCB1, we generated ABCB4-ABCB1 chimeras and tested their function in cellular PC extrusion assays. Based on a sequence alignment (Supp. Fig. 5) superimposed on the structure of ABCB4, we identified three regions of particular divergence between the two proteins (Fig. 4c): The first includes the N-terminal region of ABCB4 including TM1, the second includes the linker region between NBD1 and TMD2, and the third includes the extracellular loops. We therefore generated three chimeras: In ABCB4[B1-N-term], we replaced the N-terminus, the first elbow helix, TM1 and the first extracellular loop of ABCB4 with the corresponding segments of ABCB1. In ABCB4[B1-Linker], the linker region of ABCB4 was replaced by that of ABCB1. In ABCB4[B1-ExLoops], the extracellular loops EL1, EL3, EL4, and EL6 were spliced into ABCB4 (EL2 and EL5 are identical in the two transporters). The three chimeras were then tested for their ability to extrude PC after transient transfection into HEK cells. Given that some of the resulting constructs had different expression levels compared to WT ABCB4, the observed activities were normalized by the amounts of solubilizable protein in the plasma membranes (Supp. Fig. 7a).

In a baseline experiment, we found that WT ABCB4 extruded far greater amounts of PC than WT ABCB1 (Fig. 4d), and this difference was enhanced by the addition of taurocholate, similarly to the stimulation found using the stable cell line (Fig. 1b). We further found that both the ABCB4[B1-N-term] and the ABCB4[B1-Linker] construct had only minor effects on the activity of ABCB4 (Fig. 4d) or on the amount of protein that could be extracted from plasma membranes (Supp. Fig. 7a). However, the construct ABCB4[B1-ExLoops] displayed significantly lower extrusion activity than WT ABCB4, closer to the level of ABCB1, despite the much larger amounts of this construct expressed on the cell membrane. A residual extrusion activity remains, suggesting that the extracellular loops alone cannot fully account for the differences between ABCB4 and ABCB1.

We then considered a potential role of the hydrophobic transmembrane cavity. This cavity has been observed in many inward-facing, outward-facing, and occluded ABC transporter structures, including ABCB1[27], and was identified as the binding site of the ABCB1 inhibitor zosuquidar[44] and of the substrate paclitaxel[45]. Considering the occluded, drug-binding state of ABCB1, residues shown to interact with substrates and inhibitors are highly conserved between ABCB4 and ABCB1. Of twenty zosuquidar-binding residues, only three are not fully conserved in ABCB4 (V985, H989 and A990, Supp. Fig. 7b, Supp. Fig. 7d). We generated a triple mutant of ABCB4 (V985M, H989Q and A990V), thus converting the ABCB4 cavity to

be identical to that of ABCB1 for all the positions identified as Zosuquidar binding in ABCB1. The resulting ABCB4 variant revealed greatly reduced PC extrusion activity (Fig. 4d), comparable to exchanging all the extracellular loops (ABCB4[B1-ExLoops]). The effects of these residue exchanges could in principle be allosteric rather than direct, and rather than specifically disabling PC transport they could disable transporter function in general. However, our other chimeras show that large stretches of ABCB1 residues can be introduced into ABCB4 with little or no effect on PC extrusion, consistent with the hypothesis of a shared overall transport mechanism between ABCB1 and ABCB4 residues in general. Furthermore, for the triple mutant construct (V985M, H989Q and A990V), all nearby residues are conserved between ABCB4 and ABCB1, which makes it highly unlikely that the exchange is detrimental to transporter fold or general mechanics. A more likely interpretation of the data is therefore that these residues have a direct role in PC transport and that ABCB4 and ABCB1 both use central cavities for transporting their substrates.

Proposed transport mechanism of ABCB4

Because the residues V985, H989 and A990 proved critical for ABCB4 activity, we considered their side chain interactions in our ABCB4 structure. While the residues appear to contribute to an extensive network of interactions between the TM helices in the observed conformation, it is not evident that these interactions would be disturbed by either of the mutations V985M, H989Q or A990V (Supp. Fig. 7b). We therefore considered possible roles in other steps or states of the transport cycle. We generated homology models of ABCB4 (Fig. 5a) in distinct conformations, using as templates the outward-open state of the bacterial multidrug exporter Sav1866 (PDB: 2HYD[58]), the occluded state of human-mouse chimeric ABCB1 (PDB: 6QEE[45]), and the inward-open state of mouse ABCB1 (PDB: 4M1M[43]). In the predicted outward-open state, the side chains of the three residues V985, H989 and A990 line the outward-facing cavity and are accessible from the extracellular medium. In the predicted occluded state, they line the surface of the occluded cavity (Fig. 5c). Because these three residues were well-ordered not only in our ABCB4 structure but also in the ABCB1 structure that served as the modelling template (EMD-4281, Supp. Fig. 7d), the confidence in the modelled ABCB4 conformation is high. Finally, in the inward-open state, the three residues are accessible from the intracellular medium and from the inner leaflet of the lipid bilayer (not shown). The three residues are thus ideally positioned contribute to substrate binding and release. This is consistent with ABCB4 forming an occluded, hydrophobic cavity that constitutes the binding pocket for PC.

Discussion

ATP-driven translocation or flipping of phospholipids is an essential but mechanistically poorly understood process. Our results suggest that in contrast to mechanisms proposed for other phospholipid transporters,

ABCB4 transports PC to the outer membrane leaflet by an alternating access[27,67] mechanism, with the entire phospholipid molecule entering and leaving a central translocation pathway. This is distinct from the 'credit card swipe' mechanism proposed for active phospholipid transport by P4-ATPases[68], where the head group of the lipid is moved into or along a hydrophilic groove on the lipid-facing protein exterior while the hydrocarbon tail remains in the lipid bilayer. It is also distinct from the mechanism proposed for passive transport by scramblases of the TMEM16, which is similar to the credit card swipe model but where local distortions of the lipid bilayer geometry strongly contribute to the lowering of the activation barrier[69-72]. Yet another ABC phospholipid transporter, ABCA1, may employ an 'outward only' mechanism, similar to that employed by the lipid-linked oligosaccharide transporter PglK[32], which has as much in common with credit card swipe as with alternating access, though the details of the proposed 'lateral access' scheme for ABCA1 are not yet clear[33].

We propose that ABCB4, in contrast, employs an alternating access mechanism, similar to that proposed for multidrug export by ABCB1 but with at least two key adaptations: First, we conclude that the extracellular loops have a critical role in facilitating PC transport, potentially by assisting the reorientation of the substrate into the outer leaflet, though we cannot rule out an allosteric mode of action. Second, we show that although the residues lining the proposed translocation pathway of ABCB4 are very similar to that of ABCB1, the differences between these cavities are crucial for PC export in ABCB4. We propose that the most likely explanation for this is that the central cavity is facilitating PC transport directly. The finding that most of the cavity-forming residues are identical between ABCB4 and ABCB1 is consistent with reports that ABCB4 can recognize and transport some ABCB1 substrates. An alternating access mechanism has previously been proposed for MsbA-catalyzed transport of the lipid-A-core, a much larger molecule than phosphatidylcholine[31]. While the vanadate-trapped structure of MsbA resembles the nucleotide-bound states of ABCB4 and ABCB1[46], MsbA likely requires a different occluded state to accommodate the much larger substrate, as the inward open MsbA structure shows the substrate extending well into the cytoplasmic domain. This makes the proposed mechanism for ABCB4 unique in that it consists of relatively subtle adaptations tuning a general multi-drug export mechanism for phospholipid transport.

In conclusion, our results not only provide the first visualization of human ABCB4, they also provide insight into how a general ABC transporter architecture is adapted to different classes of substrates and different selectivity profiles. It sets the stage for studying drug-induced inhibition of ABCB4 and to delineate the precise lipid transport cycle by biophysical techniques.

Acknowledgements
JAO was supported by The Danish Council for Independent Research (grant DFF-4181-00021). Cryo-EM data was collected at the electron microscopy facility at ETH Zürich (ScopeM) and the authors thank the ScopeM staff for technical support.

Author contributions

JAO performed experiments and sample preparations. JAO and JK collected the Cryo-EM data. JAO, AA and JK processed the Cryo-EM data. JAO and KPL built and validated the model of nucleotide-bound ABCB4. JAO and KPL designed the experiments. JAO, BS and KPL conceived the project. JAO and KPL wrote the manuscript with all authors contributing to revisions.

Competing interests

The authors declare no competing interests.

Additional information

Supplementary information is available for this paper.

Data Availability

Raw data is available for figures 1b, 1d, 1e, and 4d as well as supplementary figure 2a. Coordinates for the deposited model has been deposited at The Protein Data Bank with ID 6S7P. The associated Cryo-Em map has been deposited at the Electron Microscopy Data Bank with ID EMD-10111.

References

1. Smit, J.J. et al. Homozygous disruption of the murine mdr2 P-glycoprotein gene leads to a complete absence of phospholipid from bile and to liver disease. *Cell* **75**, 451-62 (1993).
2. Morita, S.Y. & Terada, T. Molecular mechanisms for biliary phospholipid and drug efflux mediated by ABCB4 and bile salts. *Biomed Res Int* **2014**, 954781 (2014).
3. Boyer, J.L. Bile formation and secretion. *Compr Physiol* **3**, 1035-78 (2013).
4. Fagerberg, L. et al. Analysis of the human tissue-specific expression by genome-wide integration of transcriptomics and antibody-based proteomics. *Mol Cell Proteomics* **13**, 397-406 (2014).
5. Nishimura, M. & Naito, S. Tissue-specific mRNA expression profiles of human ATP-binding cassette and solute carrier transporter superfamilies. *Drug Metab Pharmacokinet* **20**, 452-77 (2005).
6. Oude Elferink, R.P. & Paulusma, C.C. Function and pathophysiological importance of ABCB4 (MDR3 P-glycoprotein). *Pflugers Arch* **453**, 601-10 (2007).
7. Lucena, J.F. et al. A multidrug resistance 3 gene mutation causing cholelithiasis, cholestasis of pregnancy, and adulthood biliary cirrhosis. *Gastroenterology* **124**, 1037-42 (2003).
8. Jacquemin, E. et al. The wide spectrum of multidrug resistance 3 deficiency: from neonatal cholestasis to cirrhosis of adulthood. *Gastroenterology* **120**, 1448-58 (2001).
9. Gautherot, J. et al. Phosphorylation of ABCB4 impacts its function: insights from disease-causing mutations. *Hepatology* **60**, 610-21 (2014).
10. Andress, E.J. et al. Molecular mechanistic explanation for the spectrum of cholestatic disease caused by the S320F variant of ABCB4. *Hepatology* **59**, 1921-31 (2014).
11. Morita, S.Y. et al. Bile salt-dependent efflux of cellular phospholipids mediated by ATP binding cassette protein B4. *Hepatology* **46**, 188-99 (2007).
12. Delaunay, J.L. et al. A functional classification of ABCB4 variations causing progressive familial intrahepatic cholestasis type 3. *Hepatology* **63**, 1620-31 (2016).
13. Delaunay, J.L. et al. Functional defect of variants in the adenosine triphosphate-binding sites of ABCB4 and their rescue by the cystic fibrosis transmembrane conductance regulator potentiator, ivacaftor (VX-770). *Hepatology* **65**, 560-570 (2017).
14. Andress, E.J., Nicolaou, M., McGeoghan, F. & Linton, K.J. ABCB4 missense mutations D243A, K435T, G535D, I490T, R545C, and S978P significantly impair the lipid floppase and likely predispose to secondary pathologies in the human population. *Cell Mol Life Sci* **74**, 2513-2524 (2017).
15. Park, H.J. et al. Functional characterization of ABCB4 mutations found in progressive familial intrahepatic cholestasis type 3. *Sci Rep* **6**, 26872 (2016).
16. Lang, C. et al. Mutations and polymorphisms in the bile salt export pump and the multidrug resistance protein 3 associated with drug-induced liver injury. *Pharmacogenet Genomics* **17**, 47-60 (2007).
17. Padda, M.S., Sanchez, M., Akhtar, A.J. & Boyer, J.L. Drug-induced cholestasis. *Hepatology* **53**, 1377-87 (2011).
18. Aleo, M.D., Shah, F., He, K., Bonin, P.D. & Rodrigues, A.D. Evaluating the Role of Multidrug Resistance Protein 3 (MDR3) Inhibition in Predicting Drug-Induced Liver Injury Using 125 Pharmaceuticals. *Chem Res Toxicol* **30**, 1219-1229 (2017).
19. He, K., Cai, L., Shi, Q., Liu, H. & Woolf, T.F. Inhibition of MDR3 Activity in Human Hepatocytes by Drugs Associated with Liver Injury. *Chem Res Toxicol* **28**, 1987-90 (2015).
20. Mahdi, Z.M., Synal-Hermanns, U., Yoker, A., Locher, K.P. & Stieger, B. Role of Multidrug Resistance Protein 3 in Antifungal-Induced Cholestasis. *Mol Pharmacol* **90**, 23-34 (2016).
21. Yoshikado, T. et al. Itraconazole-induced cholestasis: involvement of the inhibition of bile canalicular phospholipid translocator MDR3/ABCB4. *Mol Pharmacol* **79**, 241-50 (2011).
22. Reichert, M.C. & Lammert, F. ABCB4 Gene Aberrations in Human Liver Disease: An Evolving Spectrum. *Semin Liver Dis* **38**, 299-307 (2018).
23. Gudbjartsson, D.F. et al. Large-scale whole-genome sequencing of the Icelandic population. *Nat Genet* **47**, 435-44 (2015).

24. Tougeron, D., Fotsing, G., Barbu, V. & Beauchant, M. ABCB4/MDR3 gene mutations and cholangiocarcinomas. *J Hepatol* **57**, 467-8 (2012).
25. Mhatre, S. et al. Common genetic variation and risk of gallbladder cancer in India: a case-control genome-wide association study. *Lancet Oncol* **18**, 535-544 (2017).
26. Kiehl, S. et al. ABCB4 is frequently epigenetically silenced in human cancers and inhibits tumor growth. *Sci Rep* **4**, 6899 (2014).
27. Locher, K.P. Mechanistic diversity in ATP-binding cassette (ABC) transporters. *Nat Struct Mol Biol* **23**, 487-93 (2016).
28. Ruetz, S. & Gros, P. Phosphatidylcholine translocase: a physiological role for the mdr2 gene. *Cell* **77**, 1071-81 (1994).
29. Smith, A.J. et al. The human MDR3 P-glycoprotein promotes translocation of phosphatidylcholine through the plasma membrane of fibroblasts from transgenic mice. *FEBS Lett* **354**, 263-6 (1994).
30. Crawford, A.R. et al. Hepatic secretion of phospholipid vesicles in the mouse critically depends on mdr2 or MDR3 P-glycoprotein expression. Visualization by electron microscopy. *J Clin Invest* **100**, 2562-7 (1997).
31. Mi, W. et al. Structural basis of MsbA-mediated lipopolysaccharide transport. *Nature* **549**, 233-237 (2017).
32. Perez, C. et al. Structure and mechanism of an active lipid-linked oligosaccharide flippase. *Nature* **524**, 433-8 (2015).
33. Qian, H. et al. Structure of the Human Lipid Exporter ABCA1. *Cell* **169**, 1228-1239 e10 (2017).
34. Van der Bliek, A.M. et al. The human mdr3 gene encodes a novel P-glycoprotein homologue and gives rise to alternatively spliced mRNAs in liver. *EMBO J* **6**, 3325-31 (1987).
35. Smith, A.J. et al. MDR3 P-glycoprotein, a phosphatidylcholine translocase, transports several cytotoxic drugs and directly interacts with drugs as judged by interference with nucleotide trapping. *J Biol Chem* **275**, 23530-9 (2000).
36. Morita, S.Y. et al. Bile salt-stimulated phospholipid efflux mediated by ABCB4 localized in nonraft membranes. *J Lipid Res* **54**, 1221-30 (2013).
37. Wen, C. et al. Curcumin reverses doxorubicin resistance via inhibition the efflux function of ABCB4 in doxorubicinresistant breast cancer cells. *Mol Med Rep* **19**, 5162-5168 (2019).
38. Kino, K., Taguchi, Y., Yamada, K., Komano, T. & Ueda, K. Aureobasidin A, an antifungal cyclic depsipeptide antibiotic, is a substrate for both human MDR1 and MDR2/P-glycoproteins. *FEBS Lett* **399**, 29-32 (1996).
39. Duan, Z., Brakora, K.A. & Seiden, M.V. Inhibition of ABCB1 (MDR1) and ABCB4 (MDR3) expression by small interfering RNA and reversal of paclitaxel resistance in human ovarian cancer cells. *Mol Cancer Ther* **3**, 833-8 (2004).
40. Schinkel, A.H., Roelofs, E.M. & Borst, P. Characterization of the human MDR3 P-glycoprotein and its recognition by P-glycoprotein-specific monoclonal antibodies. *Cancer Res* **51**, 2628-35 (1991).
41. van Helvoort, A. et al. MDR1 P-glycoprotein is a lipid translocase of broad specificity, while MDR3 P-glycoprotein specifically translocates phosphatidylcholine. *Cell* **87**, 507-17 (1996).
42. Prescher, M., Kroll, T. & Schmitt, L. ABCB4/MDR3 in health and disease - at the crossroads of biochemistry and medicine. *Biol Chem* (2019).
43. Aller, S.G. et al. Structure of P-glycoprotein reveals a molecular basis for poly-specific drug binding. *Science* **323**, 1718-22 (2009).
44. Alam, A. et al. Structure of a zosuquidar and UIC2-bound human-mouse chimeric ABCB1. *Proc Natl Acad Sci U S A* **115**, E1973-E1982 (2018).
45. Alam, A., Kowal, J., Broude, E., Roninson, I. & Locher, K.P. Structural insight into substrate and inhibitor discrimination by human P-glycoprotein. *Science* **363**, 753-756 (2019).
46. Kim, Y. & Chen, J. Molecular structure of human P-glycoprotein in the ATP-bound, outward-facing conformation. *Science* **359**, 915-919 (2018).
47. Ishigami, M. et al. ATPase activity of nucleotide binding domains of human MDR3 in the context of MDR1. *Biochim Biophys Acta* **1831**, 683-90 (2013).
48. Groen, A. et al. Complementary functions of the flippase ATP8B1 and the floppase ABCB4 in maintaining canalicular membrane integrity. *Gastroenterology* **141**, 1927-37 e1-4 (2011).

49. Ellinger, P., Kluth, M., Stindt, J., Smits, S.H. & Schmitt, L. Detergent screening and purification of the human liver ABC transporters BSEP (ABCB11) and MDR3 (ABCB4) expressed in the yeast Pichia pastoris. *PLoS One* **8**, e60620 (2013).
50. Kluth, M. et al. A mutation within the extended X loop abolished substrate-induced ATPase activity of the human liver ATP-binding cassette (ABC) transporter MDR3. *J Biol Chem* **290**, 4896-907 (2015).
51. Higgins, C.F. & Linton, K.J. The ATP switch model for ABC transporters. *Nat Struct Mol Biol* **11**, 918-26 (2004).
52. Tombline, G., Bartholomew, L.A., Urbatsch, I.L. & Senior, A.E. Combined mutation of catalytic glutamate residues in the two nucleotide binding domains of P-glycoprotein generates a conformation that binds ATP and ADP tightly. *J Biol Chem* **279**, 31212-20 (2004).
53. Urbatsch, I.L., Sankaran, B., Weber, J. & Senior, A.E. P-glycoprotein is stably inhibited by vanadate-induced trapping of nucleotide at a single catalytic site. *J Biol Chem* **270**, 19383-90 (1995).
54. Rosenthal, P.B. & Henderson, R. Optimal determination of particle orientation, absolute hand, and contrast loss in single-particle electron cryomicroscopy. *J Mol Biol* **333**, 721-45 (2003).
55. Chovancova, E. et al. CAVER 3.0: a tool for the analysis of transport pathways in dynamic protein structures. *PLoS Comput Biol* **8**, e1002708 (2012).
56. Dimitropoulos, D., Ionides, J. & Henrick, K. Using MSDchem to search the PDB ligand dictionary. *Curr Protoc Bioinformatics* **Chapter 14**, Unit14 3 (2006).
57. Pettersen, E.F. et al. UCSF Chimera--a visualization system for exploratory research and analysis. *J Comput Chem* **25**, 1605-12 (2004).
58. Dawson, R.J. & Locher, K.P. Structure of a bacterial multidrug ABC transporter. *Nature* **443**, 180-5 (2006).
59. Choudhury, H.G. et al. Structure of an antibacterial peptide ATP-binding cassette transporter in a novel outward occluded state. *Proc Natl Acad Sci U S A* **111**, 9145-50 (2014).
60. Zaitseva, J. et al. A molecular understanding of the catalytic cycle of the nucleotide-binding domain of the ABC transporter HlyB. *Biochem Soc Trans* **33**, 990-5 (2005).
61. Esser, L. et al. Structures of the Multidrug Transporter P-glycoprotein Reveal Asymmetric ATP Binding and the Mechanism of Polyspecificity. *J Biol Chem* **292**, 446-461 (2017).
62. Hrycyna, C.A. et al. Mechanism of action of human P-glycoprotein ATPase activity. Photochemical cleavage during a catalytic transition state using orthovanadate reveals cross-talk between the two ATP sites. *J Biol Chem* **273**, 16631-4 (1998).
63. Manolaridis, I. et al. Cryo-EM structures of a human ABCG2 mutant trapped in ATP-bound and substrate-bound states. *Nature* **563**, 426 (2018).
64. Xu, D. et al. Cryo-EM structure of human lysosomal cobalamin exporter ABCD4. *Cell Res*, 2019; e-pub ahead of print 29 August 2019; doi: 10.1038/s41422-019-0222-z (2019).
65. Zhang, Z., Liu, F. & Chen, J. Conformational changes of CFTR upon phosphorylation and ATP binding. *Cell* **170**, 483-491. e8 (2017).
66. Albe, K.R., Butler, M.H. & Wright, B.E. Cellular concentrations of enzymes and their substrates. *J Theor Biol* **143**, 163-95 (1990).
67. Locher, K.P., Lee, A.T. & Rees, D.C. The E. coli BtuCD structure: a framework for ABC transporter architecture and mechanism. *Science* **296**, 1091-8 (2002).
68. Andersen, J.P. et al. P4-ATPases as Phospholipid Flippases-Structure, Function, and Enigmas. *Front Physiol* **7**, 275 (2016).
69. Brunner, J.D., Schenck, S. & Dutzler, R. Structural basis for phospholipid scrambling in the TMEM16 family. *Curr Opin Struct Biol* **39**, 61-70 (2016).
70. Falzone, M.E. et al. Structural basis of Ca(2+)-dependent activation and lipid transport by a TMEM16 scramblase. *Elife* **8**(2019).
71. Lee, B.C. et al. Gating mechanism of the extracellular entry to the lipid pathway in a TMEM16 scramblase. *Nat Commun* **9**, 3251 (2018).
72. Malvezzi, M. et al. Out-of-the-groove transport of lipids by TMEM16 and GPCR scramblases. *Proc Natl Acad Sci U S A* **115**, E7033-E7042 (2018).

73. Schneider, C.A., Rasband, W.S. & Eliceiri, K.W. NIH Image to ImageJ: 25 years of image analysis. *Nat Methods* **9**, 671-5 (2012).
74. Chifflet, S., Torriglia, A., Chiesa, R. & Tolosa, S. A method for the determination of inorganic phosphate in the presence of labile organic phosphate and high concentrations of protein: application to lens ATPases. *Anal Biochem* **168**, 1-4 (1988).
75. Zheng, S.Q. et al. MotionCor2: anisotropic correction of beam-induced motion for improved cryo-electron microscopy. *Nat Methods* **14**, 331-332 (2017).
76. Zhang, K. Gctf: Real-time CTF determination and correction. *J Struct Biol* **193**, 1-12 (2016).
77. Scheres, S.H. RELION: implementation of a Bayesian approach to cryo-EM structure determination. *J Struct Biol* **180**, 519-30 (2012).
78. Zivanov, J. et al. New tools for automated high-resolution cryo-EM structure determination in RELION-3. *Elife* **7**(2018).
79. Punjani, A., Rubinstein, J.L., Fleet, D.J. & Brubaker, M.A. cryoSPARC: algorithms for rapid unsupervised cryo-EM structure determination. *Nat Methods* **14**, 290-296 (2017).
80. Emsley, P., Lohkamp, B., Scott, W.G. & Cowtan, K. Features and development of Coot. *Acta Crystallogr D Biol Crystallogr* **66**, 486-501 (2010).
81. Adams, P.D. et al. PHENIX: a comprehensive Python-based system for macromolecular structure solution. *Acta Crystallogr D Biol Crystallogr* **66**, 213-21 (2010).
82. Waterhouse, A. et al. SWISS-MODEL: homology modelling of protein structures and complexes. *Nucleic Acids Res* **46**, W296-W303 (2018).
83. Ho, B.K. & Gruswitz, F. HOLLOW: generating accurate representations of channel and interior surfaces in molecular structures. *BMC Struct Biol* **8**, 49 (2008).

Online methods

Generation of expression constructs. A DNA sequence coding for the predominant isoform of ABCB4 (UniProt ID P21439-2) was designed with regularly spaced silent restriction sites, codon optimized for expression in human cells and generated synthetically (Thermo Fischer Scientific). All subsequent modifications of the sequence, including the introduction of the point mutations E558Q and E1200Q, were performed using synthetic gene fragments (Integrated DNA technologies). Restriction enzymes and T4 DNA ligase were purchased from NEB. Constructs for transient expression in HEK293 cells were cloned, following the strategy described above, into an expression vector containing the pXLG gene expression cassette in a pUC57 vector. Stable cell lines for expression were generated using the Flp-In T-Rex system (Thermo Fisher Scientific), according to the manufacturer's guidelines. All expression constructs included a C-terminal eYFP/rho-ID4 tag and a preceding 3C protease cleavage site. ABCB4-ABCB1 chimeras were constructed with ABCB1 residues exchanged into ABCB4 as follows: ABCB4[B1-N-term]: residues 1-109. ABCB4[B1-Linker]: residues 630-716. ABCB4[B1-ExLoops]: residues 92-109, 324-334, 737-753 and 963-971.

Protein production and purification. Flp-In T-Rex 293 cells stably expressing ABCB4 or ABCB4[EQ] were adapted to grow in suspension culture in EX-Cell 293 serum-free medium (Sigma-Aldrich) supplemented with 100 Units/ml Penicillin, 100ug/ml Streptomycin and 6mM Glutamine. Cells were maintained at 37°C and shaking at 100rpm (Kuhner) at 6% CO_2 and 80% humidity. Expression was induced by addition of 0.25ug/ml tetracycline (AppliChem). Cells were harvested after 48-72 hours by spinning at 6000 rpm in an F-10S rotor (Thermo Scientific) for 10 min. All subsequent steps were performed at 4°C or on ice unless otherwise specified. Cell pellets were resuspended in 150mM NaCl, 20mM HEPES pH 7.5 and 20% glycerol (4ml/g pellet) supplemented with cOmplete EDTA-free protease inhibitor cocktail tablets (Roche) and homogenized using a dounce homogenizer. Protein was solubilized by addition of a mixture of 1% dodecyl maltopyranoside (DDM) and 0.2% cholesteryl hemisuccinate (CHS) and incubation on a roller shaker for 90 minutes. Cellular debris and non-solubilized membrane fragments were spun down for 30 min at 35000 rpm in a Type 45-Ti rotor (Beckmann). The supernatant was applied to sepharose-coupled Rho-ID4 antibody (University of British Columbia) and incubated for at least 1 hour. Beads were washed four times with ten column volumes (CV) of buffer (as during resuspension) supplemented with 0.02%/0.004% DDM/CHS. Subsequently, beads were incubated for at least one hour with 3 CV buffer supplemented with a 1:10 (w/w) ratio of 3C protease to protein. Cleaved protein was eluted through Ni-NTA beads (Qiagen) for capturing the His-tagged protease. Protein concentrations in detergent micelles were measured by absorbance at 280nm using a NanoDrop 2000c spectrophotometer (Thermo Fischer Scientific)

Nanodisc reconstitution. A mixture of liver polar lipids from (LPL) from Avanti Polar lipids and CHS (4:1 w/w) were solubilized in 0.5% DDM/CHS and mixed with nanodisc scaffold protein MSP1D1 and ABCB4 in

a stoichiometry of 20:1:0.2, diluted to reduce glycerol concentration below 4% and incubated 15min at RT. CHS was chosen over cholesterol as this was necessary to fully solubilize the lipid mix prior to reconstitution. However, it is noted that LPL already contains 5% cholesterol. Nanodisc formation was induced by removing detergent with Bio-Beads (Bio-Rad) for 2H at room temperature. Samples were concentrated on 100k MWCO centrifugal filter. Protein concentrations in nanodiscs were measured by gel densitometry analysed in imageJ[73].

ATPase activity assays. Hydrolysis of ATP was measured with a molybdate based colorimetric assay[74]. 5-10ug of protein in detergent (150mM NaCl, 20mM HEPES pH 7.5, 20% glycerol and 0.02%/0.005% DDM/CHS) or 3-7ug embedded in LPL:CHS nanodiscs (150mM NaCl and 20mM HEPES pH 7.5) were used per reaction. Assays were started by addition of ATP in the presence of 10mM $MgCl_2$, incubated for 30-40min at 37°C, and stopped by addition of 6% SDS. Control reactions in the absence of $MgCl_2$ were run in duplicate and subtracted as background for each data point. Reactions were done in triplicate and repeated with different batches of protein and reagents. Results were analysed in GraphPad Prism 7.

PC efflux assays. Flp-In T-Rex 293 cells carrying a gene for stable expression of ABCB4 or ABCB4[EQ], or HEK293T cells, were grown in adherent culture plates in DMEM medium supplemented with 10% FBS and penicillin/streptomycin at 37 °C at 6% CO_2 in a humidified incubator. Flp-In T-Rex cells were induced to expression by exchange into DMEM supplemented with 2% FBS, penicillin/streptomycin and 0.2µg/ml tetracycline. HEK 293T cells were transiently transfected in DMEM supplemented with 2% FBS and penicillin/streptomycin by dropwise addition of a mixture of DNA and branched polyethylenimine (1:2.5 ratio). After 24H expression, cells were washed with PBS and medium was exchanged to DMEM supplemented with 0.02% BSA, with or without 0.1mM Na-taurocholate. After a further 18H, medium was harvested, lipids were extracted with a 40:20:1 methanol:chloroform:0.1M KCl mixture and dried under argon. PC content was analyzed with Phosphatidylcholine Assay Kit (SIGMA). Total cellular protein was measured with Pierce BCA Protein Assay Kit (Thermo). Curve fitting was done in GraphPad Prism 7. At least three experiments were performed in duplicate for each sample, except for the ABCB4[EQ] stable cell line where two experiments were performed in duplicate. To estimate expression levels, DDM/CHS solubilized, fluorescently labelled protein was extracted from pelleted cells and analysed on a TSKgel G4000SWXL column at 0.5ml/min (0.4ml/min for protein extracted from stably expressing cells) in 150mM NaCl, 20mM HEPES pH 7.5 and 0.02%/0.004% DDM/CHS. Results from cells transiently expressing different constructs were normalized relative to expression level of each construct and was shown relative to results for ABCB4 without added NaTc, measured on the same batch of cells. Results from stable cell lines were normalized according to total cellular protein.

EM sample preparation. WT ABCB4 or ABCB4[EQ] reconstituted into LPL:CHS nanodiscs was loaded on a TSKgel G3000SWxl column (Tosh Biosciences) and run in a 150mM NaCl, 20mM HEPES pH 7.5 buffer at

0.4ml/min. The peak fraction, at ~0.5mg/ml, was equilibrated with either 5mM ATP and 5mM $MgCl_2$ (ABCB4[EQ]) or 4mM ATP, 10mM $MgCl_2$ and 4mM Na_3VO_4 (WT ABCB4) before blotting for 3 seconds on glow-discharged Quantifoil carbon grids (1.2/1.3µM, 300 mesh, copper) using a Vitrobot Mark IV (FEI). Grids were plunge-frozen into a liquid ethane-propane mixture cooled by liquid nitrogen.

Cryo-EM data acquisition and processing. Grids were imaged with a Titan Krios (FEI) electron microscope operating at 300 keV and equipped with a Gatan Quantum LS energy filter (GIF) and a Gatan K2 Summit direct electron detector. Image stacks comprising 40 Frames were collected in super resolution mode at a nominal magnification of 165000x.

For data collection using the ABCB4[EQ] sample with ATP and Mg^{2+} an estimated dose rate of 1.7 electrons per square angstrom per frame was applied. Defocus was set to vary from −0.5 to −3µm. A total of 6865 micrograph stacks were motion-corrected, dose-weighted and two-fold Fourier-cropped to a calibrated pixel size of 0.84Å in MotionCor2[75] (Supp. Figure 3a). Contrast Transfer Function was estimated with gCTF[76]. From 5124 micrographs selected after CTF estimation, a total of 1815578 particles were picked in RELION[77,78] using a 3D template generated from an initial model, which in turn was calculated from particles picked by the Laplacian-of-Gaussian based autopicking procedure on all selected micrographs. After two rounds of 2D classification, initial 3D classification was performed with three classes. A majority of particles (71%) located to closed conformations and a minority of particles into a conformation with more separation between the NBDs. For particles belonging to the more open class processing did not improve the density beyond a reported 8Å resolution (Supp. Fig. 3b). Most likely this class contains particles with a spectrum of NBD separation. Particles from the highest quality of the closed classes were refined using RELION's 3D auto-refine procedure and post processed to 3.4Å. Subsequent 3D classification into two classes in RELION resulted in a 3D class containing the majority of particles (193929 particles) and which had slightly stronger signal for the NBDs and helices and slightly weaker signal for the nanodisc compared to the other class. Refinement and postprocessing of this class yielded a 3.3Å map. CTF refinement, Bayesian Polishing within RELION and exclusion of the nanodisc region from the map yielded the final 3.2Å resolution structure, as estimated based on the FSC cutoff criterion of 0.143 (Supp. Fig. 3c). This map was subsequently used for model building.

For data collection using the WT ABCB4 sample with ATP, MG^{2+} and NA_3VO_4 (Supp. Fig. 2b-d) an estimated dose rate of 1 electron per square angstrom per frame was applied. Defocus was set to vary from −1 to −3µm. A total of 2630 micrograph stacks were motion-corrected, dose-weighted and two-fold Fourier-cropped to a calibrated pixel size of 0.84Å in MotionCor2 and the Contrast Transfer Function was estimated with gCTF. From 1421 micrographs selected after CTF estimation, a total of 215840 particles were picked using Gautomatch (http://www.mrc-lmb.cam.ac.uk/kzhang/) and processed in cryoSPARC[79]. 138724 particles were selected after one round of 2D classification. Heterogeneous refinement with three classes

produced two classes with greater NBD separation while the class with the greatest number of particles (38%, 53171 particles) showed less NBD separation. Further refinement did not lead to improved map quality (Supp. Fig. 2d).

Model building and refinement. The B-factor sharpened map at 3.2Å was used for model building in Coot[80] with the quality of density in most of the TMDs and NBDs allowing for *de-novo* model building (Supp. Fig. 4). A model was built for ABCB4 in the nucleotide-bound state (Fig. 2a-b) and comprising residues 42-84, 105-629 and 692-1252. For both residues H589 and H1231 density indicated the presence of two orientations also affecting surrounding residues and in each case the orientation with the strongest density was built into the model. Coordinate refinement was performed in Phenix[81] with geometric and secondary structure restraints. Residue numbers in the paper are based on human ABCB4 isoform 2 (UniProt ID P21439-2).

Homology modelling. Homology models were generated in SWISS-MODEL[82] based on templates 2HYD, 6QEE and 4M1M. Residues 1-40 and 630-691 were excluded from the final models as good templates for these regions were unavailable.

Figure preparation. Images of models and maps were prepared in UCSF Chimera[57] and PyMOL (The PyMOL Molecular Graphics System, Version 2.0 Schrödinger, LLC).

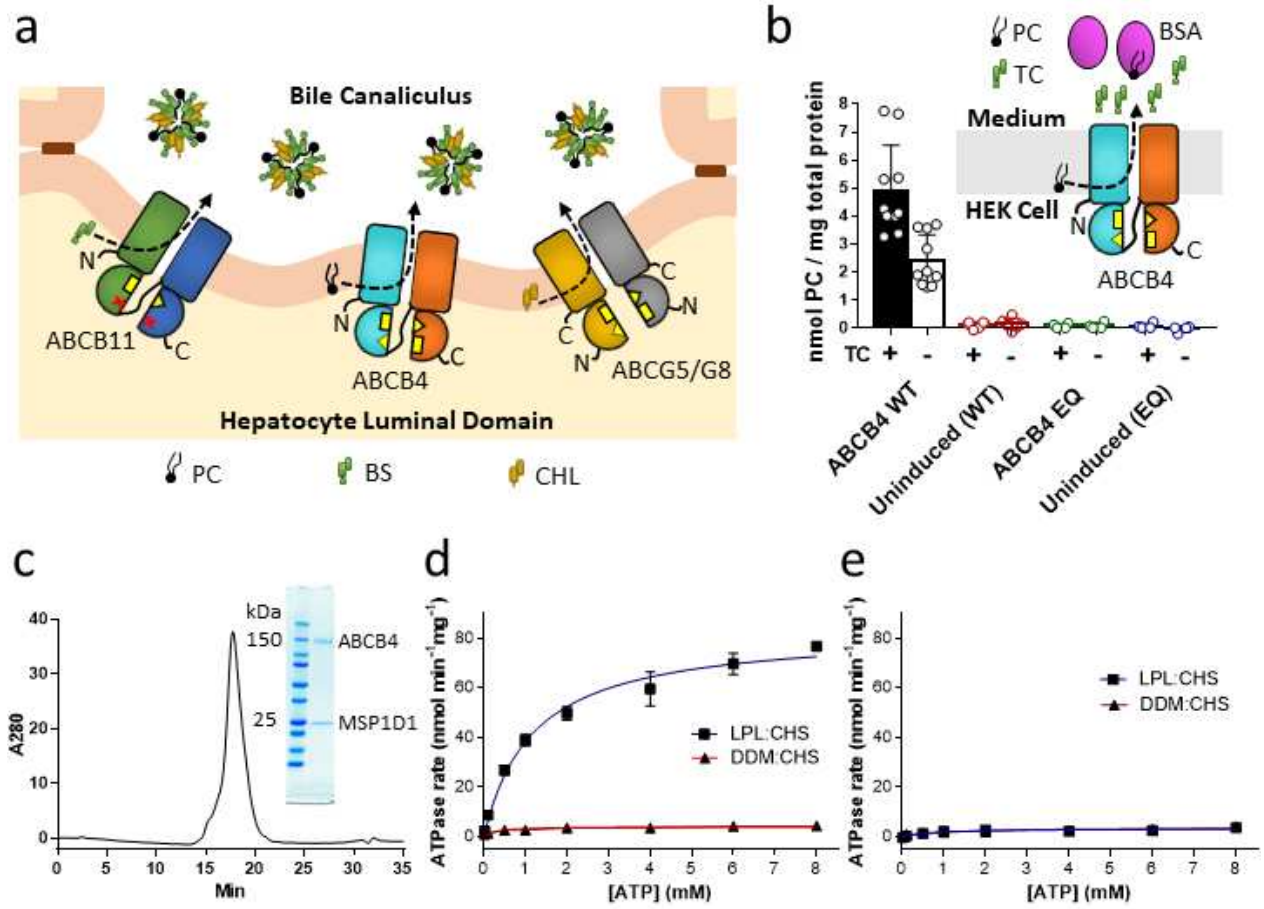

Figure 1. Functional characterization of ABCB4. **a)** Schematic of PC extrusion in the bile canaliculi. PC indicates phosphatidylcholine, BS bile salt and CHL cholesterol. Tight junctions are indicated in brown, between hepatocytes. Yellow rectangles and triangles indicate complementary sides of nucleotide binding sites. **b)** PC extrusion by WT ABCB4 and ABCB4[EQ] stably expressed in Flp-In T-REx 293 cells. Filled bars indicate extrusion in the presence of 1mM sodium taurocholate while unfilled bars indicate extrusion in the absence of taurocholate. Error bars indicate S.E.M of the data points shown. Insert shows schematic of PC extrusion from HEK293T cells expressing ABCB4. TC indicates taurocholate, BSA indicates bovine serum albumin. **c)** SEC profile of purified WT ABCB4 reconstituted into LPL:CHS nanodiscs. The inset shows sample loaded on SDS-PAGE, with bands for ABCB4 (theoretical MW 141kDa) and the nanodisc scaffold protein MSP1D1 (theoretical MW 24.7kDa). **d)** ATPase activity of ABCB4 in a lipid environment (LPL:CHS nanodiscs, black squares, curve fitted to Michaelis-Menten kinetics in blue), and in detergent (DDM/CHS micelles, black triangles, red curve). Data points indicate means of three independent measurements, error bars indicate S.E.M. **e)** ATPase activity of the ABCB4[EQ] double mutant in nanodiscs (black squares, blue curve) and DDM/CHS (black triangles, red curve). Data points indicate means of three independent measurements, error bars indicate S.E.M.

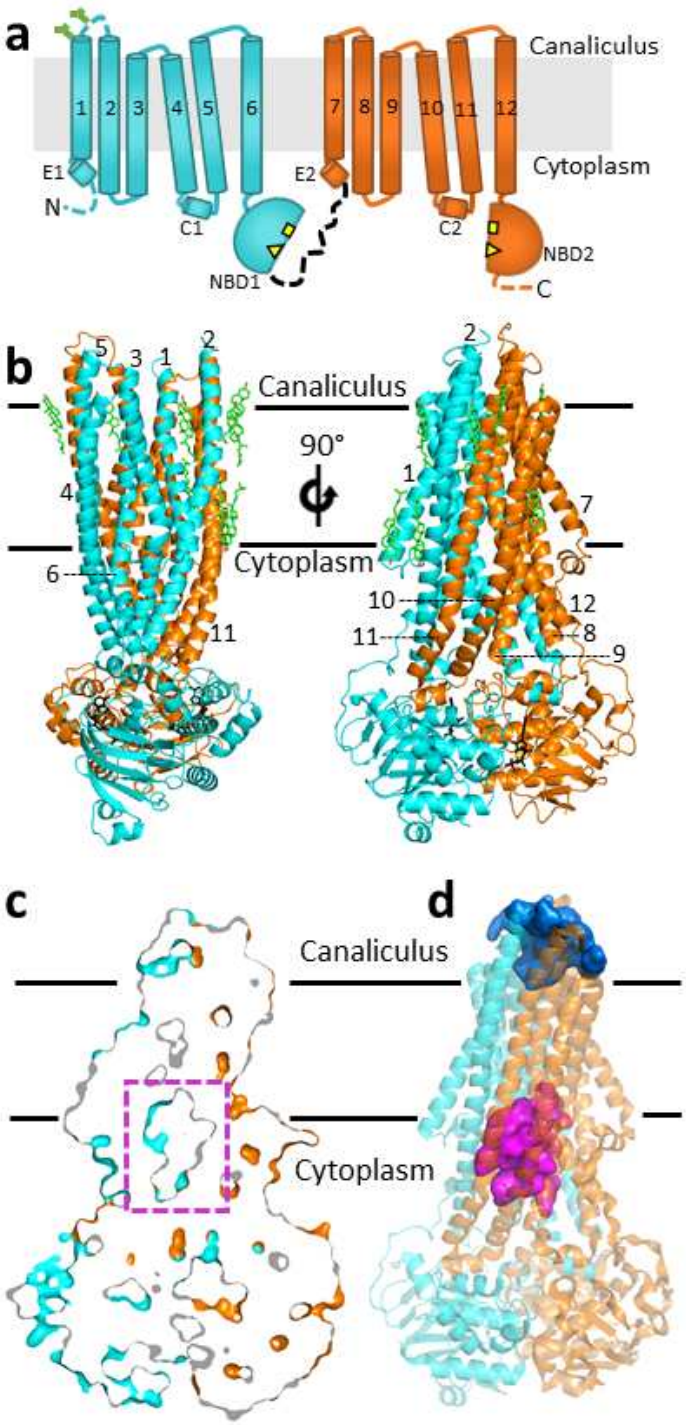

Figure 2. Structure of human ABCB4. **a)** Topology diagram of ABCB4. Transmembrane helices are numbered. Elbow helices (E1 and E2) are indicated as are the coupling helices (C1 and C2) and the NBDs. Stretches of residues not built in the final model are indicated with dotted lines. Predicted N-glycosylation sites indicated in green, ATP-binding sites in yellow. **b)** Cartoon representation our ABCB4 model with the first half of the sequence, including transmembrane helices (TMHs) 1-6 and NBD1, coloured cyan and the second half, including TMHs7-12 and NBD2, coloured in orange. Nucleotides are represented as black sticks, Mg^{2+} as a yellow sphere and cholesterol as green sticks. **c)** Surface representation of ABCB4 oriented as in the right side of panel b) with view clipped to a thickness of ~2Å around the centre of the protein. The hydrophilic cavity is indicated by dashed magenta rectangle. **d)** The central cavity (magenta) and the top cavity/surface (blue) are visualized with Hollow[83] inside a translucent cartoon representation of ABCB4.

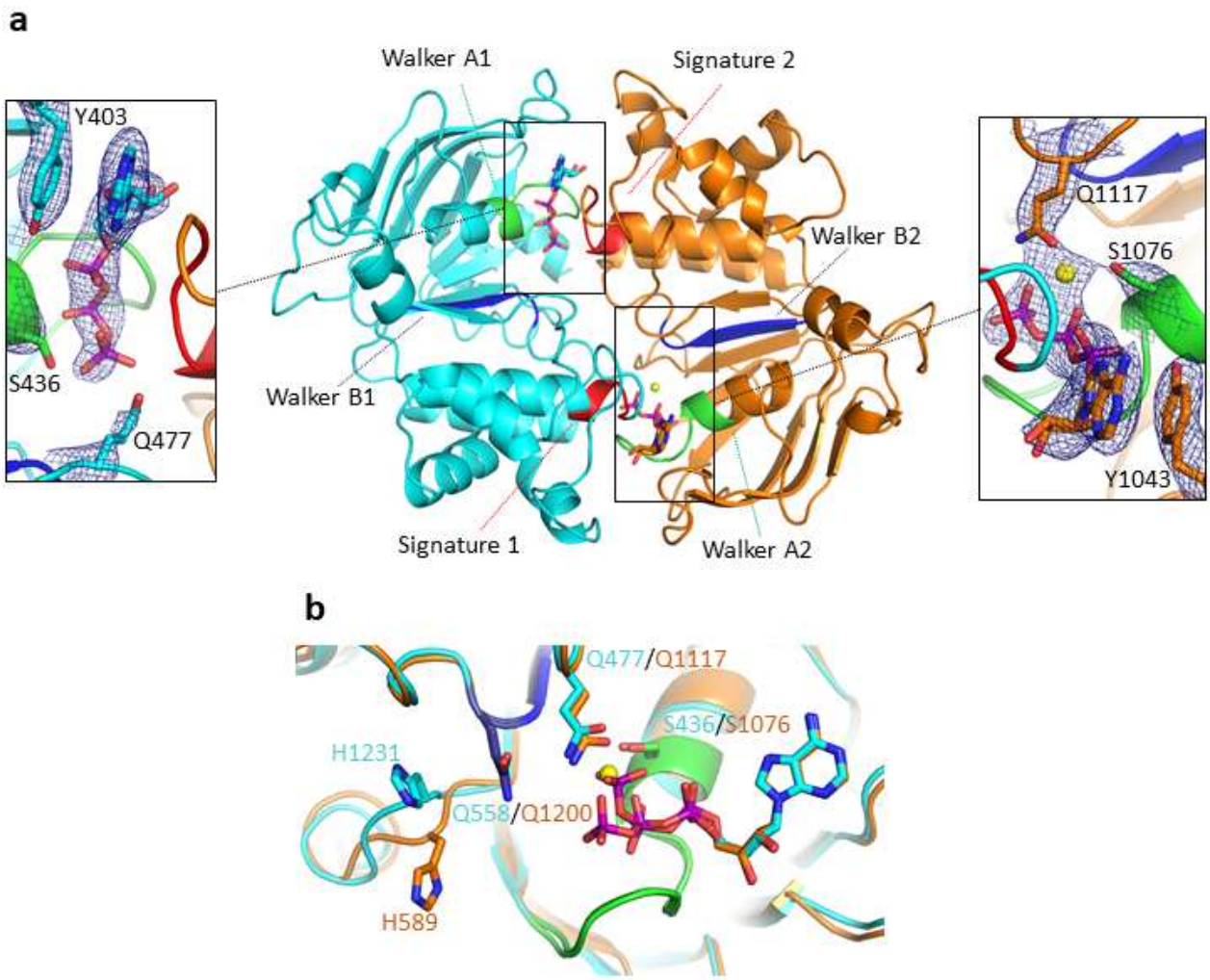

Figure 3. Nucleotide binding to ABCB4. **a)** Cartoon representation of the NBDs viewed from the direction of the membrane toward the cytoplasm with inserts showing density of nucleotides and selected residues for each site, contoured at σ =10 and carved at a distance of 2Å. **b**) The two half-NBDs are shown superimposed upon each other, with interacting nucleotides and selected residues shown in stick format and magnesium as a yellow sphere. Colouring of atoms follows panel a), with carbon atoms coloured according to structural elements, phosphorous coloured purple, nitrogen blue and oxygen red.

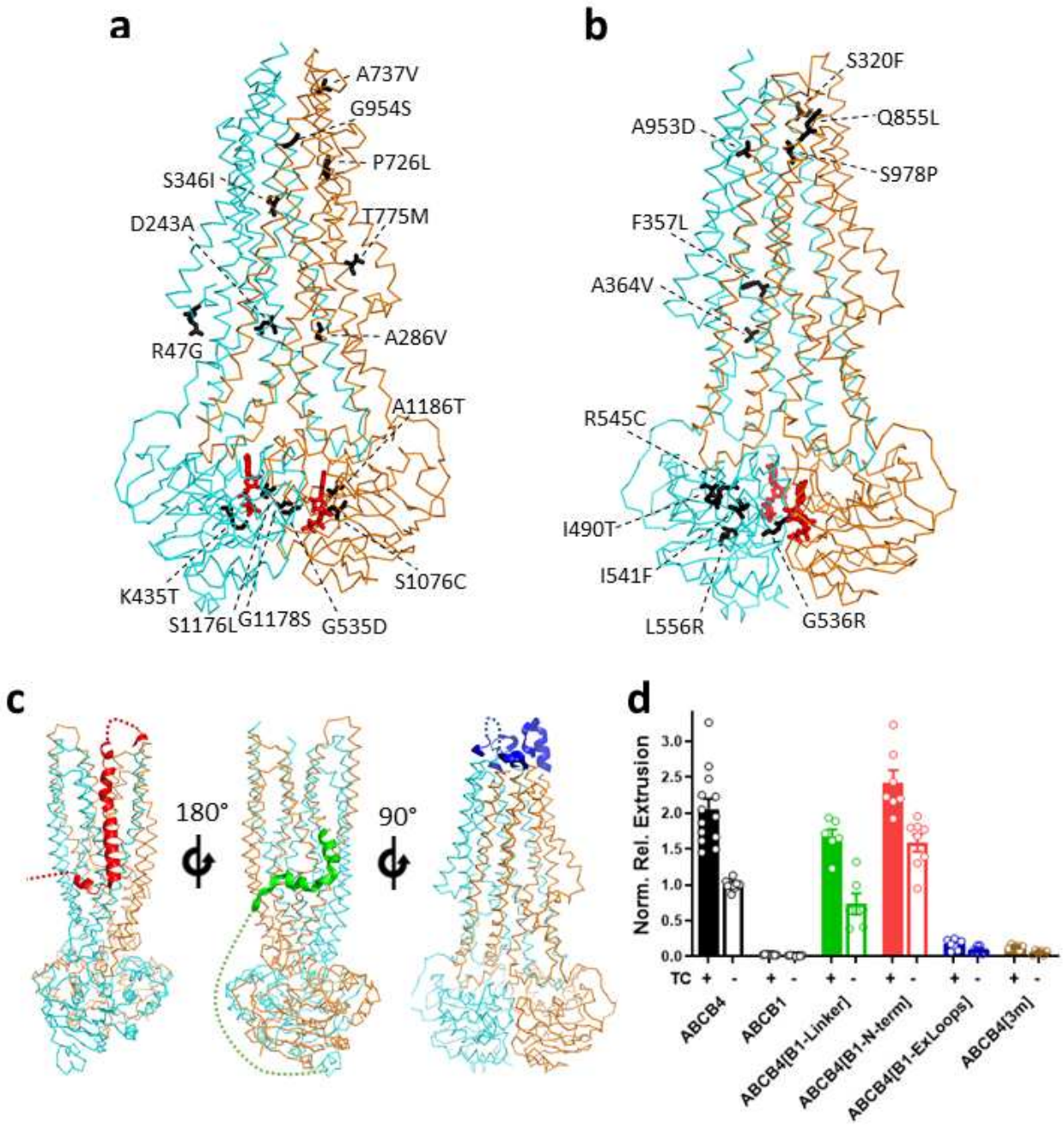

Figure 4. Functionally impairing mutants and chimeras of ABCB4. **a)** Disease causing mutations functionally impairing ABCB4 are shown in black on a ribbon representation of ABCB4. ATP shown in red. **b)** Disease causing mutations impairing maturation or trafficking of ABCB4 are shown in black. **c)** Ribbon representation of ABCB4 with the regions of greatest sequence variability between ABCB4 and ABCB1 indicated as cartoons in respectively Green (ABCB4[B1-N-term]), Red (ABCB4[B1-Linker]) and Blue (ABCB4[B1-ExLoops]). Dashed lines indicate residues not resolved in the present structure. **d)** PC extrusion by ABCB4-ABCB1 chimeras in transiently transfected HEK cells with (solid bars) and without (hollow bars) stimulation of extrusion by 0.1mM NaTc. Error bars indicate S.E.M. the data points shown. Results are normalized to according to amount of transporter extracted from membranes (Supp. Fig. 4a) and shown relative to WT ABCB4 without taurocholate.

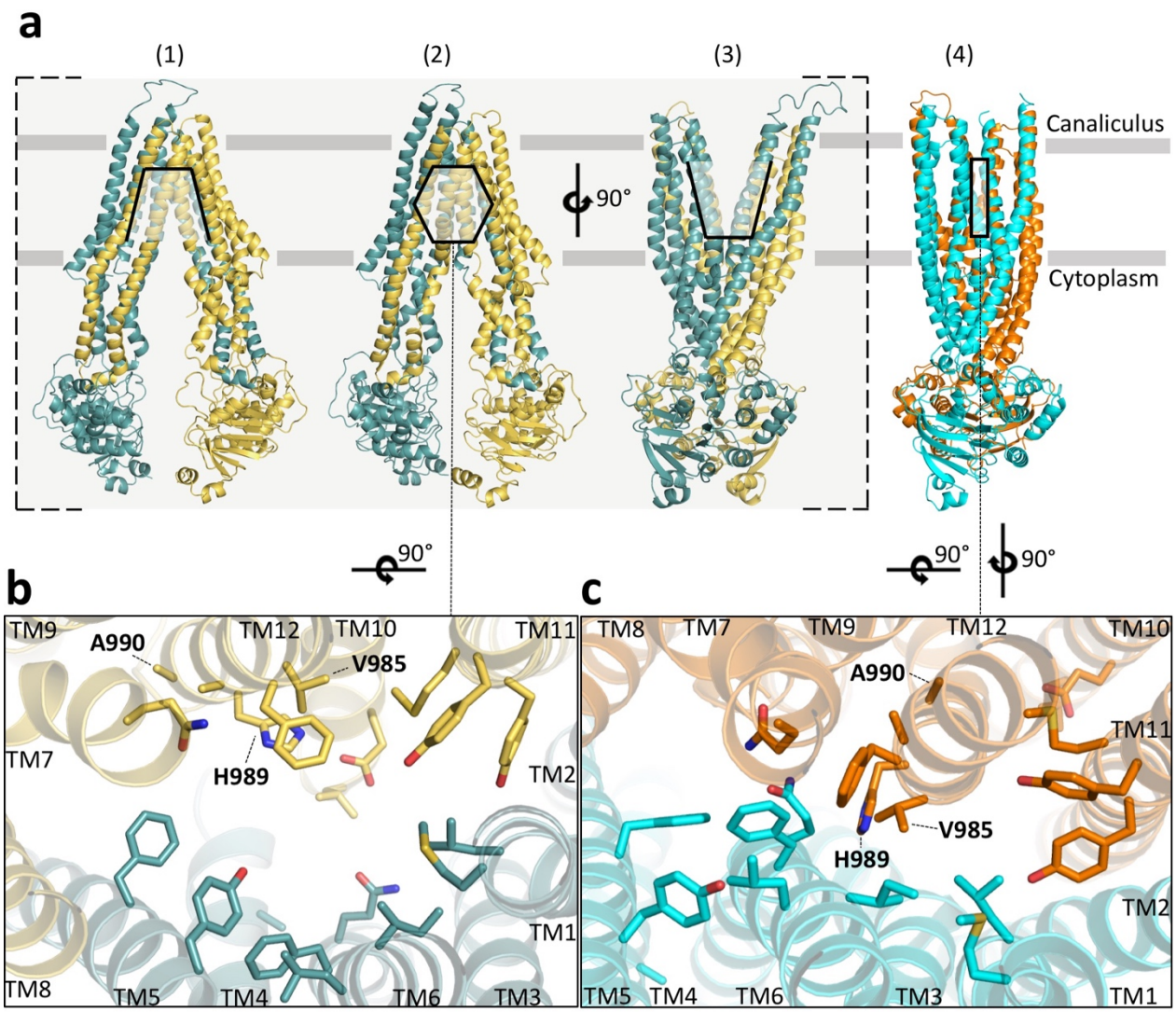

Figure 5. The structure of ABCB4 in the context of the transport cycle. **a)** Our structure of the closed conformation of ABCB4 (4) is shown next to homology models based on (1) inward open ABCB1 (PDB 4M1M), (2) inward occluded ABCB1 (PDB 6QEE) and (3) outward open Sav1866 (PDB 2HYD). **b)** Predicted occluded state of ABCB4, with residues predicted to interact with compounds bound in the hydrophobic cavity shown as sticks. Viewed from the direction of the canaliculus. **c)** The nucleotide bound state of ABCB4 is shown with the same residues as in b shown as sticks.

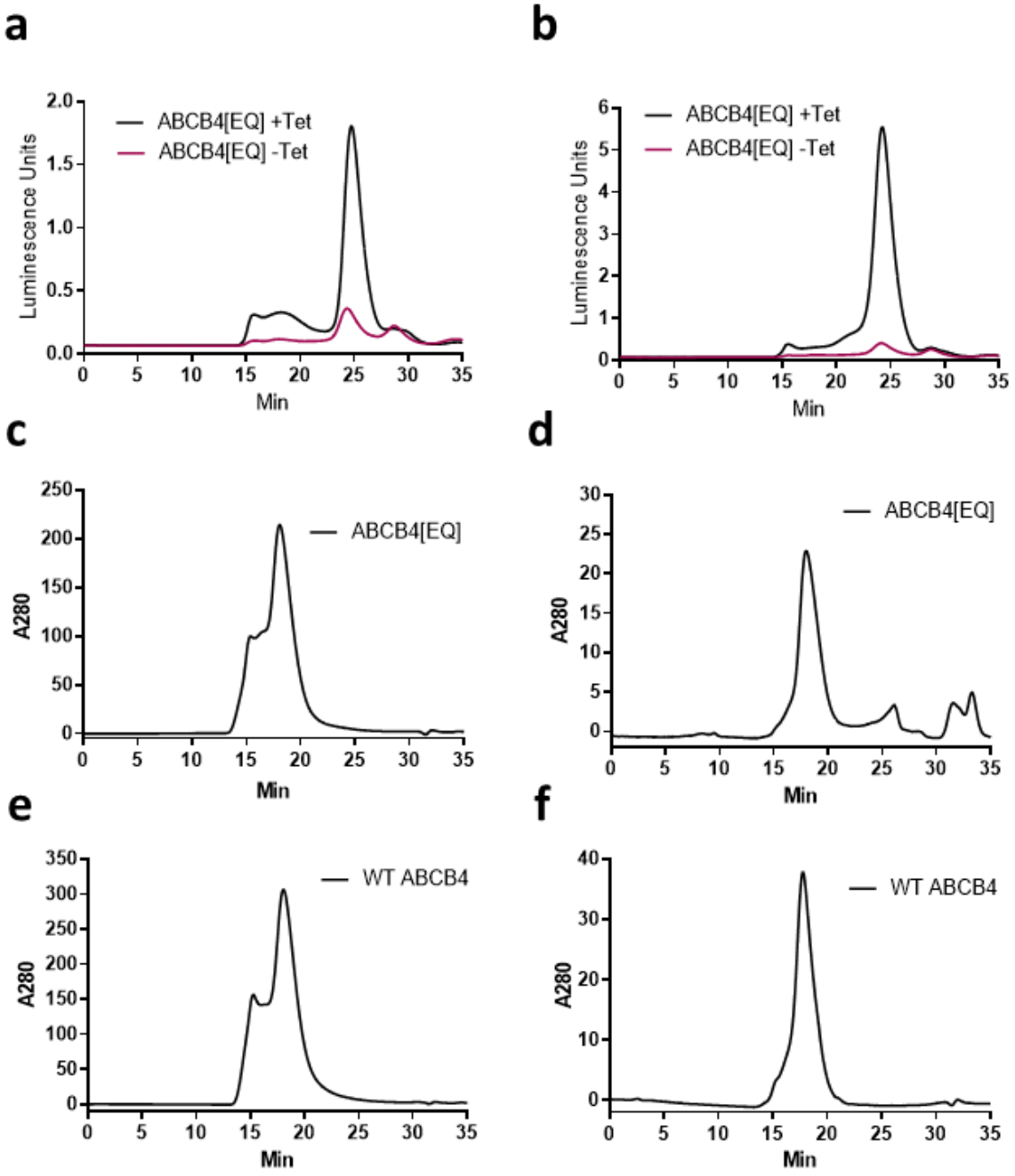

Supplementary Figure 1. A-b) FSEC profiles of eYFP-labeled protein extracted by DDM/CHS from pellets of WT ABCB4 expressing Flp-In T-Rex 293 cells collected after harvesting of media for extrusion experiments. Black lines indicates signal from cell with expression induced by addition of tetracycline, red lines indicates signal from uninduced cells. Samples were loaded on a TSKgel G4000SWXL column at 0.4ml/min. a) Signals from cells expressing wt-ABCB4). B) Signals from cells expressing ABCB4[EQ]. c-f) SEC profiles of purified ABCB4 reconstituted into LPL:CHS nanodiscs and run on a a TSKgel G3000SWXL column at 0.4ml/min. c) ABCB4[EQ] d) Reinjection of the peak from c) at around 18min. e) *wt*-ABCB4 with reinjected peak fraction shown in f), as also shown in Fig. 1c.

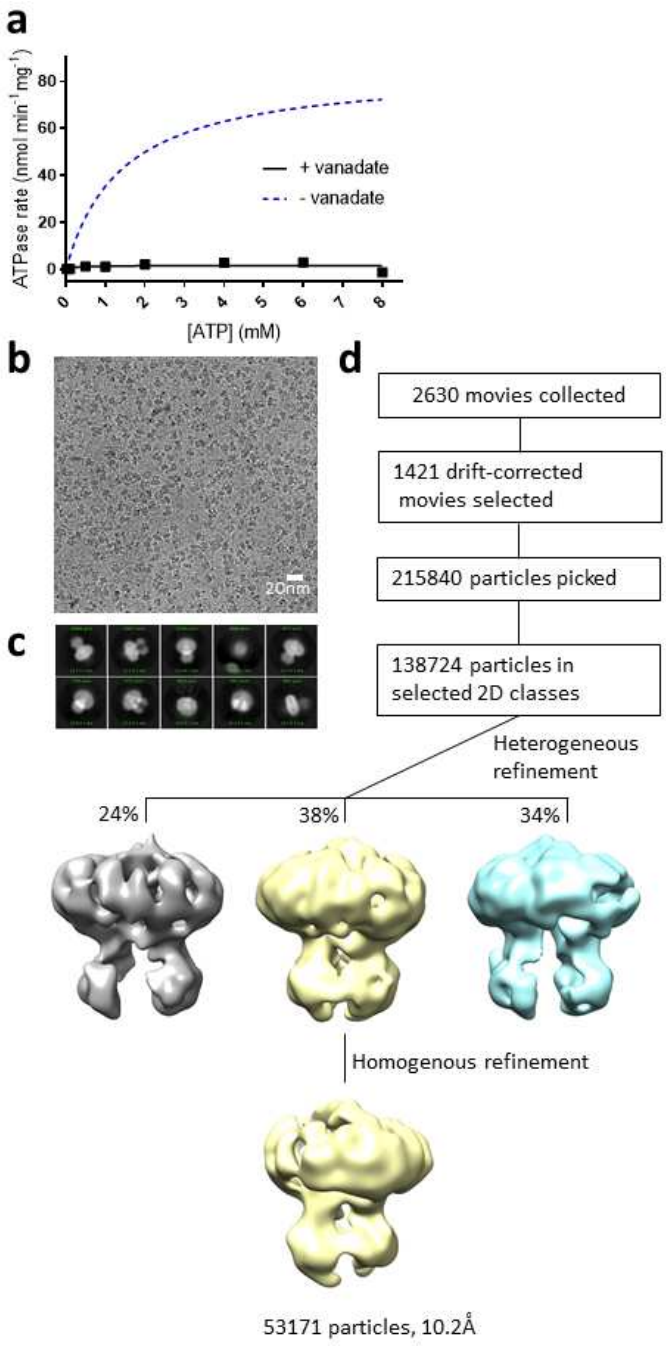

Supplementary Figure 2. Cryo-EM data processing of vanadate-trapped *wt*-ABCB4. **a)** ATPase activity of vanadate-trapped *wt*-ABCB4 (black squares and curve) shown relative to the activity without vanadate (dashed blue line, curve from fig. 1d). Data points indicate means of three independent measurements, error bars represent S.E.M. **b)** Representative motion-corrected micrograph of ABCB4 at a nominal magnification of 165kx and a defocus of 2.7 µm. **c)** Representative 2D classes from cryoSPARC. **d)** cryoSPARC processing workflow.

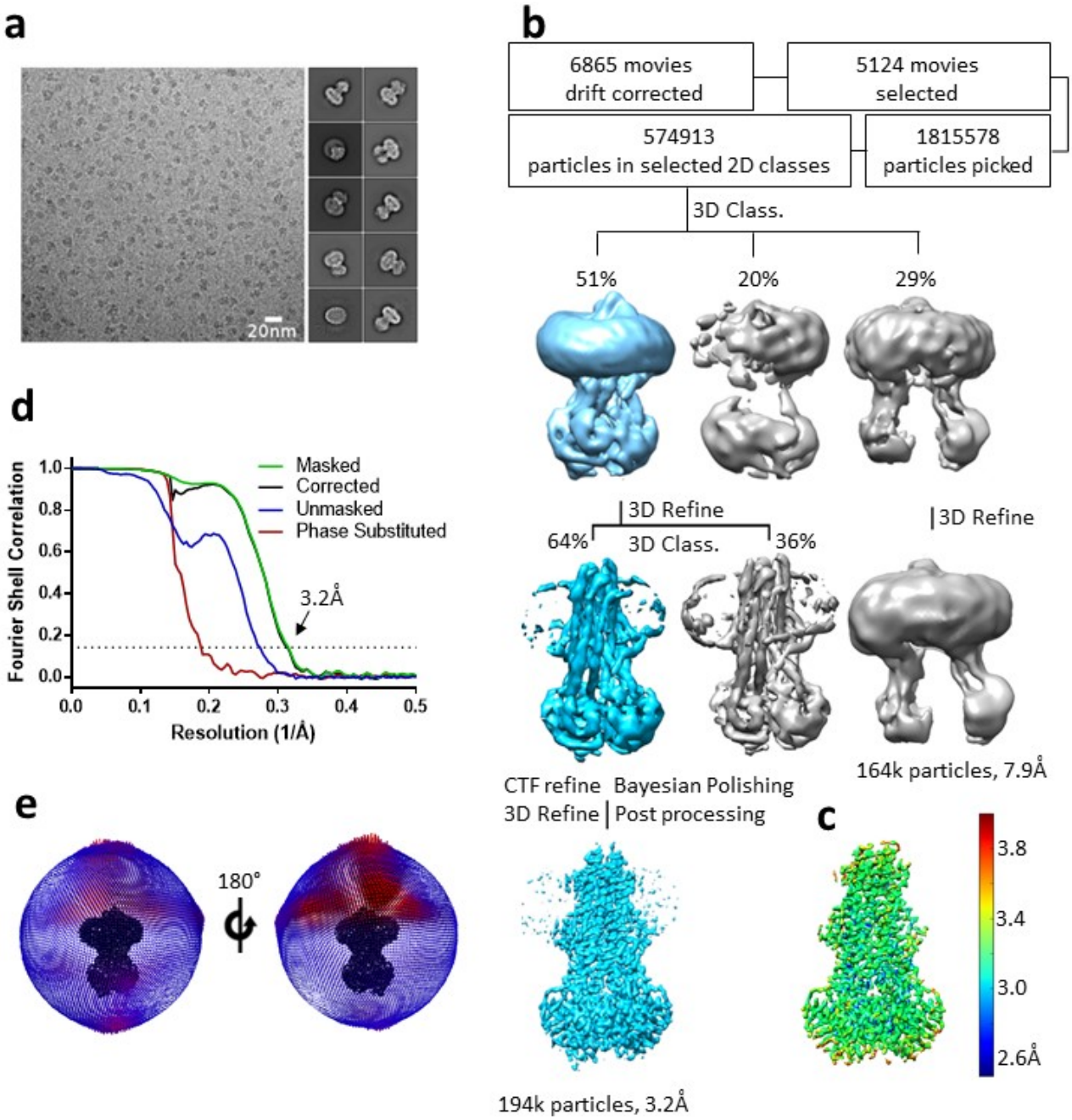

Supplementary Figure 3. Cryo-EM structure determination of nucleotide-bound ABCB4. **a)** Representative motion-corrected micrograph of ABCB4 at nominal magnification of 165kx and a defocus of 2.2µm. Representative 2D classes from RELION are shown to the left. **b)** RELION processing workflow **c)** Local resolution calculated with ResMap in RELION and presented on the sharpened EM map, colour coded according to the scale bar next to the density. **d)** Fourier shell correlation curves from RELION. **e)** Distribution of orientations of particles going into the final class.

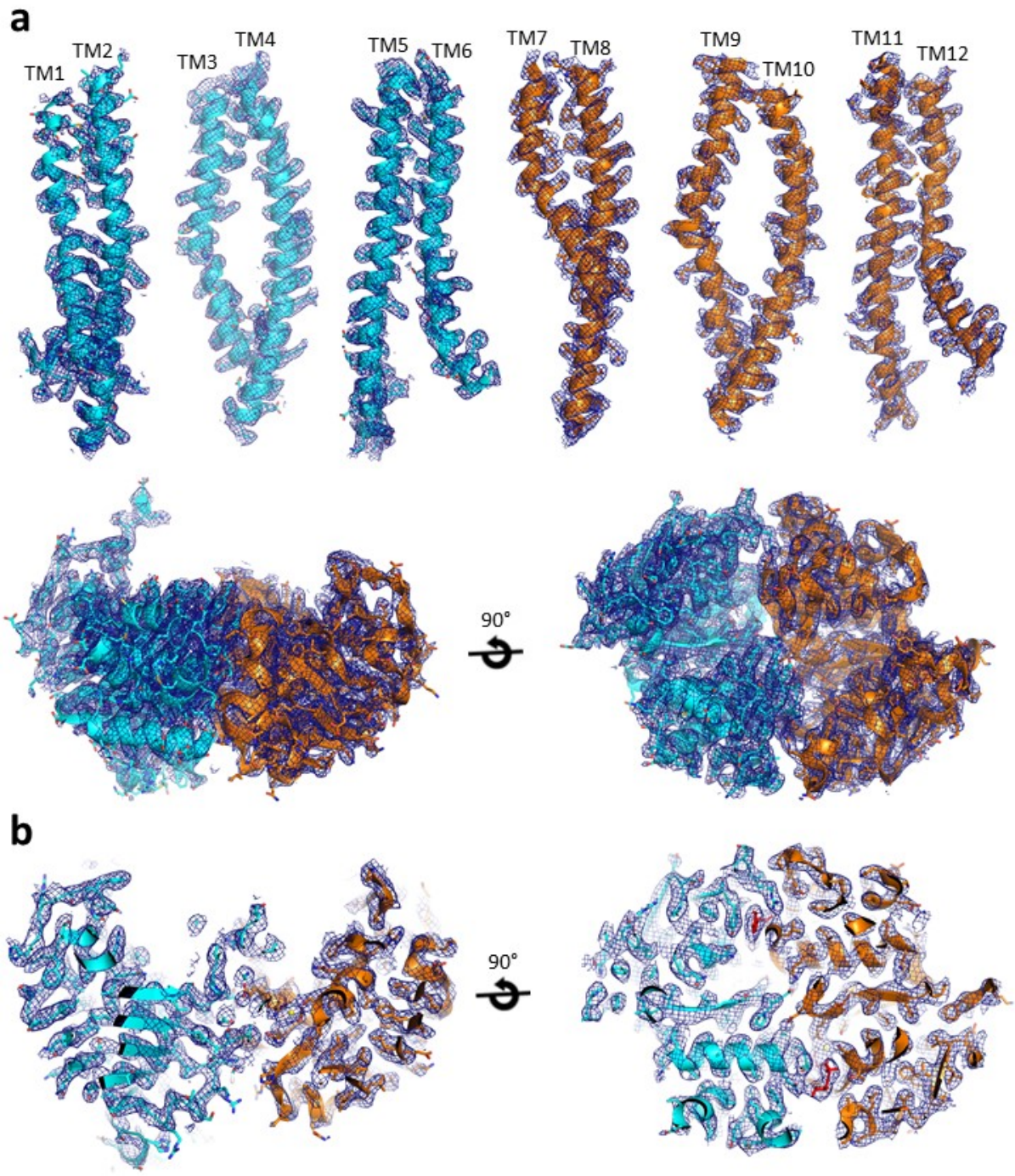

Supplementary Figure 4. The model of nucleotide-bound ABCB4 built according to density. Contour level is set at σ =5 and density is carved at a distance of 2Å. **a)** Density contours from b-factor sharpened map is shown for all six helix pairs as well as the NBDs. **b)** Density contours shown around central slices of the NBDs, for the same views as shown in a). Nucleotides are shown in red, Magnesium in yellow.

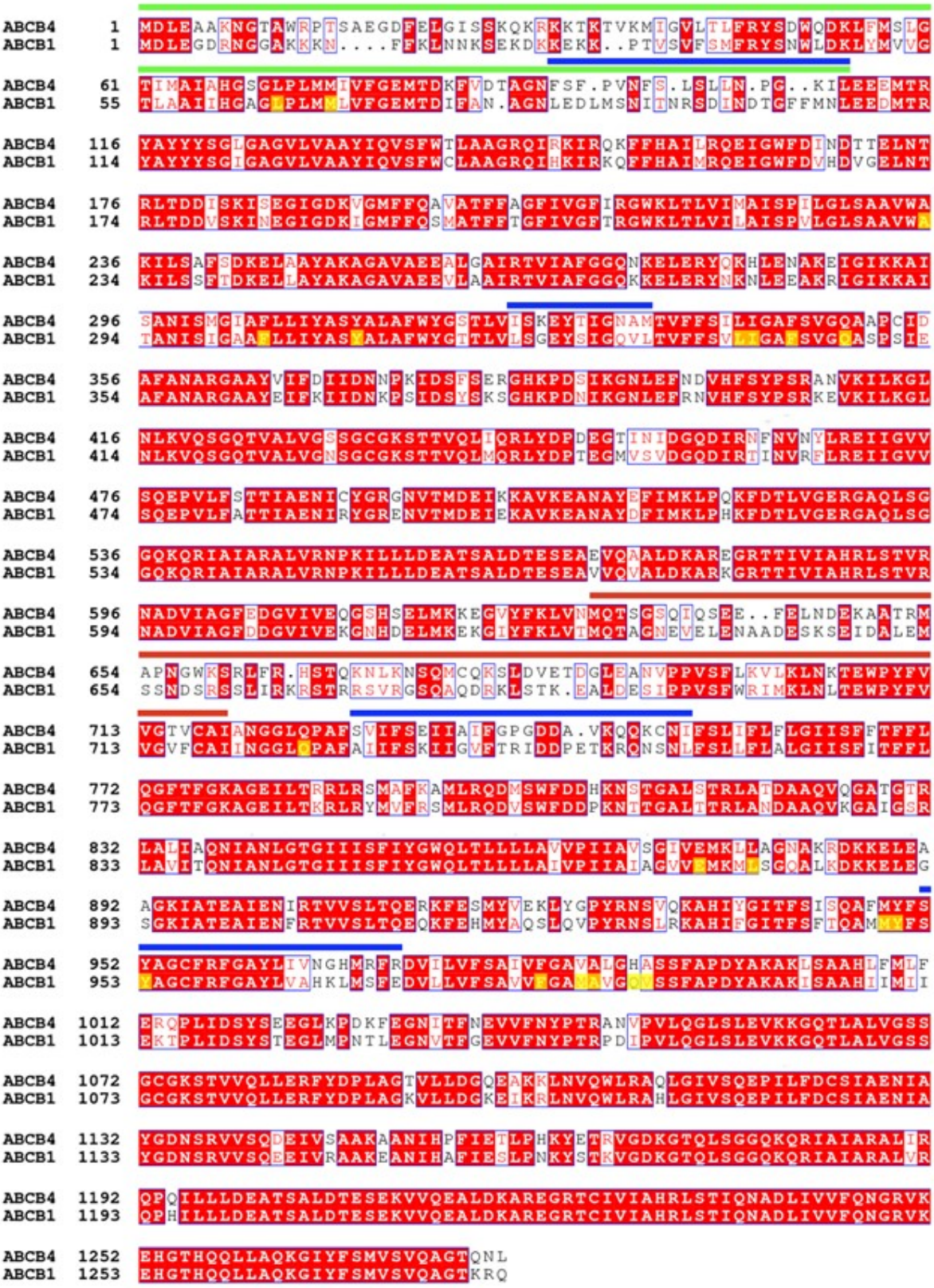

Supplementary Figure 5. Alignment between human ABCB4 and ABCB1. Sequence alignment was done in T-Coffee and layout was done using the ENDscript server. ABCB1 residues interacting with inhibitor zosuquidar are highlighted in yellow. Residues exchanged in chimeric constructs are indicated with bars coloured as in Fig. 4b.

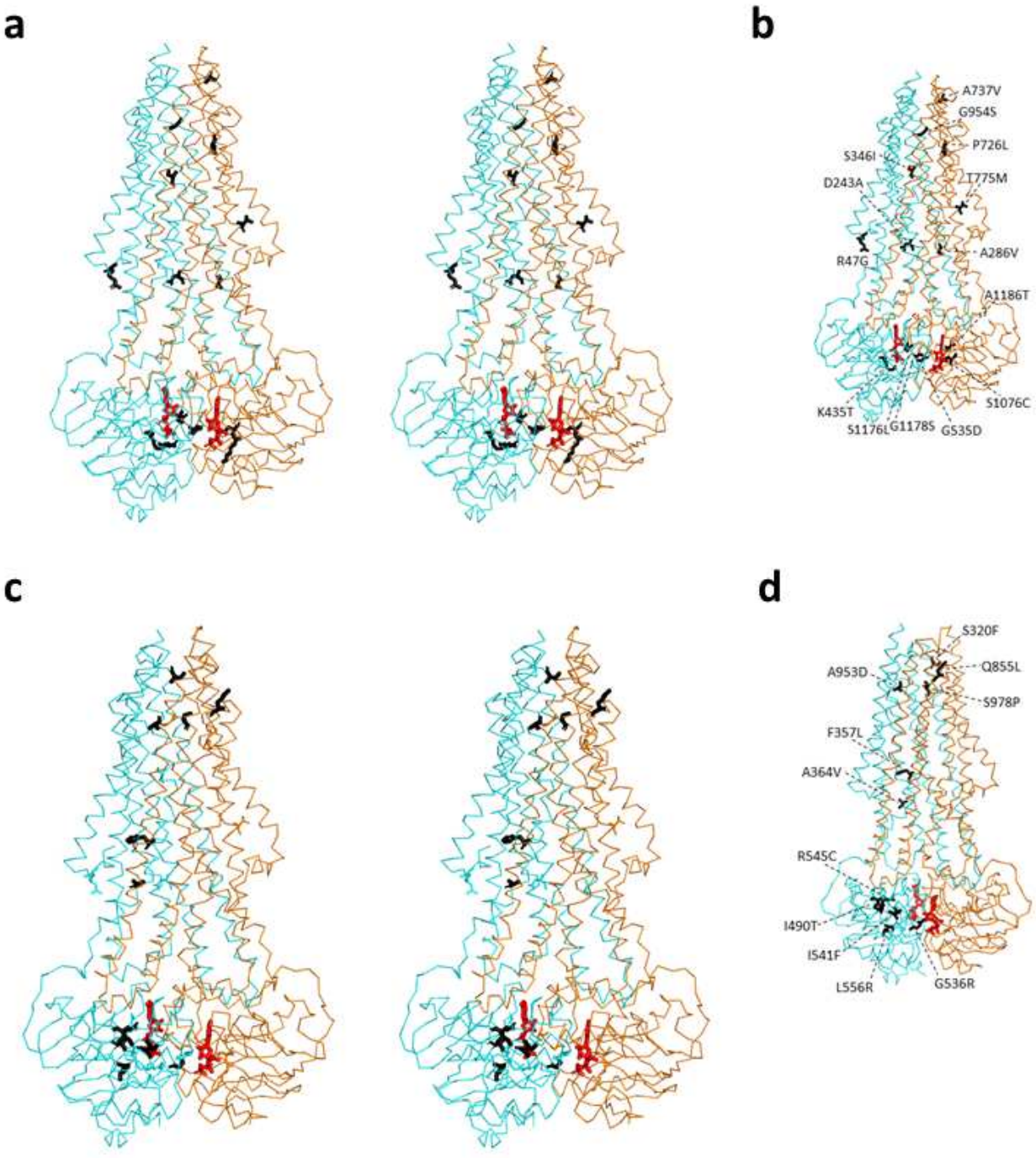

Supplementary Figure 6. Stereo representations from PyMOL of disease causing mutants of ABCB4 mapped onto the closed conformation described in this work**. A)** Mutations affecting function. **B)** For clarity, panel a of main figure 4 is shown with residue identities indicated. **C)** Mutations affecting expression or trafficking. **D)** Panel b of main figure 4 is shown with residue identities labelled.

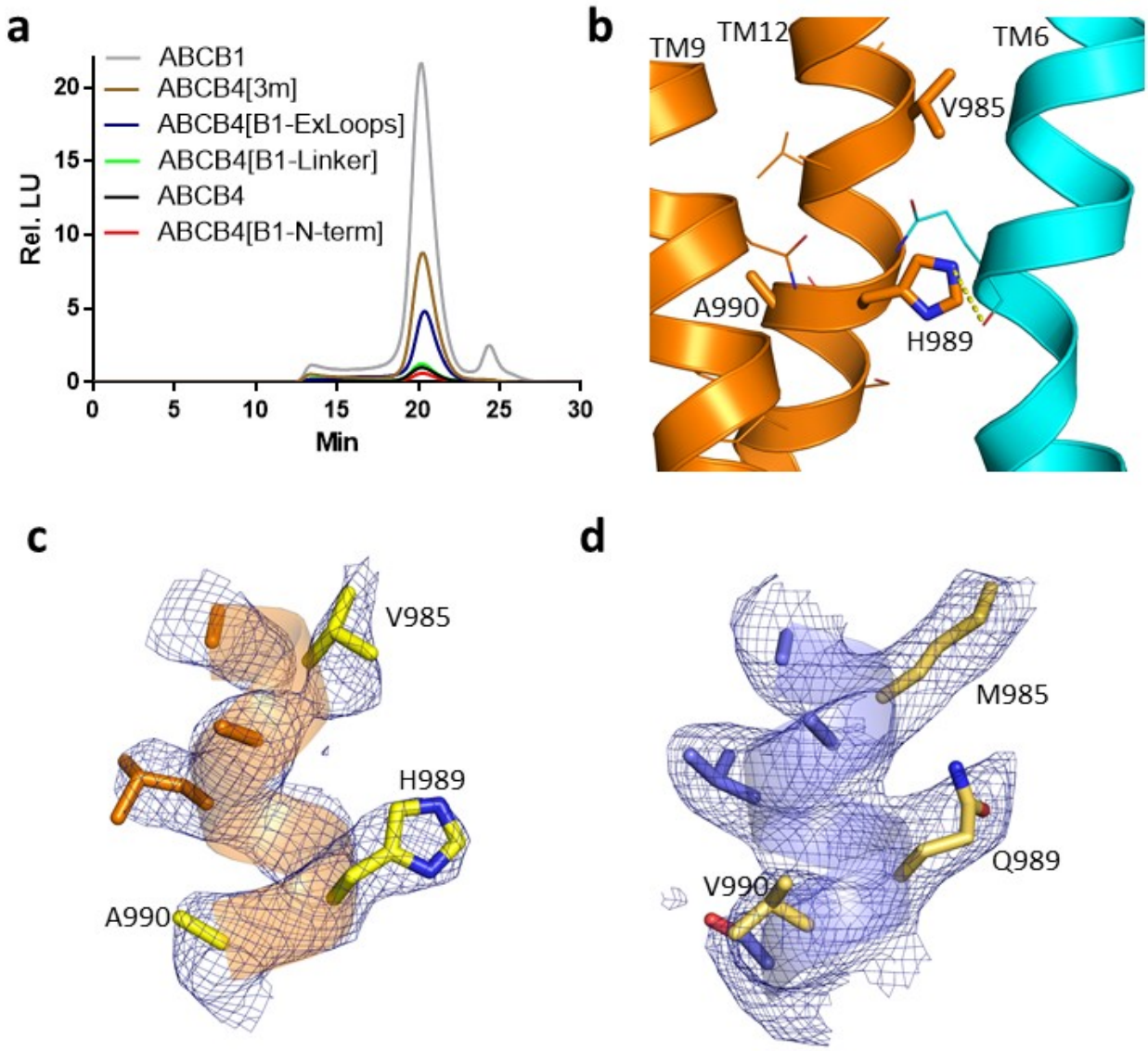

Supplementary Figure 7. a) ABCB4 and ABCB1 chimeras reveal important residues. The amounts of protein extracted with DDM/CHS from experiments shown in Fig. 4d are indicated by luminescence units relative to *wt*-ABCB4. Main peak heights (peak at 20 min) were used to normalize results of the extrusion assays. **b)** The three positions mutated in the 3M construct (V985M, H989Q and A990V) are shown in a model of the ATP-Mg^{2+} bound ABCB4 in stick representation, and residues within 4Å are shown in line representation. **c)** Residues V985, H989 and A990 and nearby residues on TMH12, from the model of ABCB4 in the closed conformation, are shown with associated density contoured at a level of σ =6.5 and carved at a distance of 2Å from residues. d**)** Residue positions corresponding to those in a) are shown on the previously published model of human-mouse chimeric ABCB1 bound to the inhibitor zosuquidar[44], used for homology modelling, with density from the associated map contoured at a level of σ =6.5 and carved at a distance of 2Å from residues.

Cryo-electron microscopy data collection and processing	
Microscope	FEI Titan Krios
Voltage (keV)	300
Camera	Gatan K2-Summit
Energy Filter	Gatan Quantum-LS (GIF)
Pixel size (Å)	0.84
Defocus range (μm)	(-0.5) - (-2.5)
Number of micrographs	6865
Particles in final class	193929
Resolution (Å)	3.2
Sharpening B-factor ($Å^2$)	-85.4
Coordinate refinement and validation	
Number of protein atoms (non-H)	8741
Number of ligand atoms (non-H)	287
RMSD bonds (Å)	0.009
RMSD angles (°)	1.034
Ramachandran favored (%)	97.24
Ramachandran Allowed (%)	2.76
Ramachandran Disallowed (%)	0
All-atom clashscore	3.49
Rotamer outliers (%)	0.33

Supplementary Table 1. Overview of EM data collection and coordinate refinement with statistics from MolProbity in Phenix.

	Mutation	Function (% of WT)*	Rel. protein on plasma membrane	Disease association
Mutations affecting function	T34M	58.3% ± 6.6%[9]	~100%[9]	BC, DILI, ICP, LPAC[9, 84]
	R47G	32.2% ± 5.6%[9]	~100%[9]	LPAC[84, 85]
	D243A	56% ± 0.16%[14]	~100%[14]	BC[86]
	A286V	~0%[10]	~100%[10]	LPAC, PFIC3[89]
	S346I	~5%[12***]	~100%[12***]	PFIC3[89]
	K435T	~0%[14]	~100%[14]	BC[86]
	G535D	~0%[14], ~20% [13***]	~100%[14]	BC, CG, ICP[88]
	P726L	~5%[12***]	~100%[14]	PFIC3[89]
	A737V	53%[15**]	~100%[15]	PFIC3[89]
	T775M	~75%[12***]	~100%[12***]	PFIC3[89]
	G954S	~60%[12***]	~100%[12***]	PFIC3[89]
	S1076C	~10%[13***]	~100%[13]	PFIC3[92]
	S1176L	~5%[13***]	~100%[13]	LPAC[13]
	G1178S	~2%[13***]	~100%[13]	LPAC[13]
	A1193T	61%[15**]	~100%[15]	PFIC3[89]
Mutations affecting function	S320F	~100%[10]	50.1%[10]	DILI[90], ICP[90], LPAC[89], PFIC3[89]
	F357L	~40%[12***]	~25%[12***]	PFIC3[89]
	A364V	51%[15**]	30%[15]	PFIC3[89]
	I490T	N.D.[14]	6%[14]	CC, CG, JD, PR[87]
	G536R	~2%[13]	~55%[13***]	ICP[93]
	I541F	~10%[12***]	Only immature form expressed[12]	PFIC3[89]
	R545C	N.D.[14]	17%[14]	SC[86]
	L556R	~10%[12***]	Only immature form expressed[12]	PFIC3[89]
	Q855L	~40%[12***]	~60%[12***]	PFIC3[89]
	S978P	N.D.[14]	22%[14]	CC, ICP, LPAC[87]
	A953D	29%[10]	16.3%[10]	PFIC3[91]

Supplementary Table 2. Overview of disease causing mutations of ABCB4 referred to in this paper. *BC:* Biliary Cirrhosis, *DILI:* Drug-induced Liver Injury, *ICP:* Intrahepatic Cholestasis of Pregnancy, *LPAC:* Low-Phospholipid–Associated Cholelithiasis, *SC:* Sclerosing Cholangitis, *CC:* Cholangiocarcinoma, *CG:* Cholesterol Gallstones, *JD:* Jaundice, *PR:* Pruritus, *PFIC3:* Progressive Familial Intrahepatic Cholestasis Type 3, *N.D:* Not Detected. *: Normalized to expression level relative to WT. **: Value refers to ATPase activity rather than transport. ***Value estimated visaully from graph in reference.

References

84. Wendum, D. et al. Aspects of liver pathology in adult patients with MDR3/ABCB4 gene mutations. *Virchows Arch* **460**, 291-298 (2012).
85. Poupon, R. et al. Genotype-phenotype relationships in the low-phospholipid-associated cholelithiasis syndrome: a study of 156 consecutive patients. *Hepatology* **58**, 1105-1110 (2013).
86. Pauli-Magnus, C. et al. BSEP and MDR3 haplotype structure in healthy Caucasians, primary biliary cirrhosis and primary sclerosing cholangitis. *Hepatology* **39**, 779-791 (2004).
87. Tougeron, D., Fotsing, G., Barbu, V. & Beauchant, M. ABCB4/MDR3 gene mutations and cholangiocarcinomas. *J Hepatol* **57**, 467-468 (2012).
88. Lucena, J.-F. et al. A multidrug resistance 3 gene mutation causing cholelithiasis, cholestasis of pregnancy, and adulthood biliary cirrhosis. *Gastroenterology* **124**, 1037-1042 (2003).
89. Degiorgio, D. et al. Molecular characterization and structural implications of 25 new ABCB4 mutations in progressive familial intrahepatic cholestasis type 3 (PFIC3). *Eur J Hum Genet* **15**, 1230 (2007).
90. Rosmorduc, O., Poupon, R. & Hermelin, B. MDR3 gene defect in adults with symptomatic intrahepatic and gallbladder cholesterol cholelithiasis. *Gastroenterology* **120**, 1459-1467 (2001).
91. Keitel, V. et al. Expression and localization of hepatobiliary transport proteins in progressive familial intrahepatic cholestasis. *Hepatology* **41**, 1160-1172 (2005).
92. Davit-Spraul, A., Gonzales, E., Baussan, C. & Jacquemin, E. The spectrum of liver diseases related to ABCB4 gene mutations: pathophysiology and clinical aspects. in *Seminars in liver disease* Vol. 30 134-146 (Thieme Medical Publishers, 2010).
93. Floreani, A. et al. Hepatobiliary phospholipid transporter ABCB4, MDR3 gene variants in a large cohort of Italian women with intrahepatic cholestasis of pregnancy. *Dig Liver Dis* **40**, 366-370 (2008).